

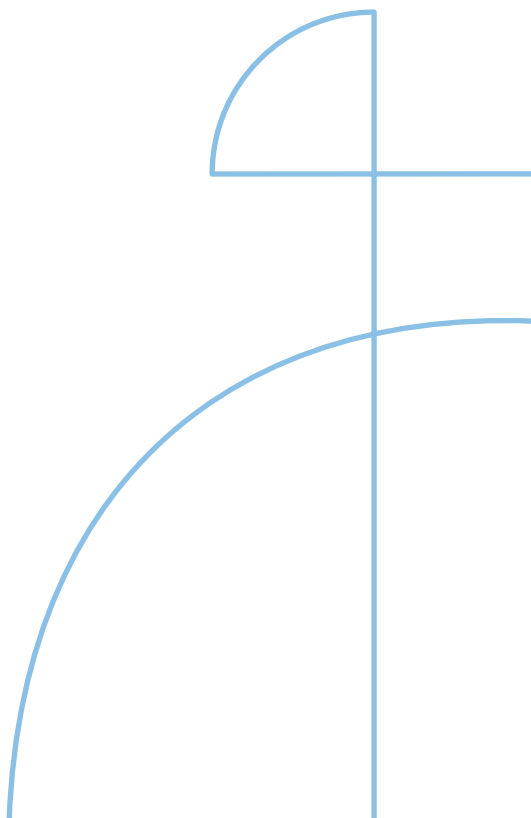


Doctoral Thesis in Chemical Engineering

# Lithium-ion battery performance and degradation in stationary energy storage

MATHILDA OHRELIUS

KTH ROYAL INSTITUTE OF TECHNOLOGY



# Lithium-ion battery performance and degradation in stationary energy storage

MATHILDA OHRELIUS

Academic Dissertation which, with due permission of the KTH Royal Institute of Technology, is submitted for public defence for the Degree of Doctor of Philosophy on Friday the 22nd November 2024, at 10:00 a.m. in K1, Teknikringen 56, Stockholm.

Doctoral Thesis in Chemical Engineering  
KTH Royal Institute of Technology  
Stockholm, Sweden 2024

© Mathilda Ohrelus

TRITA-CBH-FOU-2024:47  
ISBN 978-91-8106-099-7

Printed by: Universitetservice US-AB, Sweden 2024

# Abstract

Electrification is our most promising strategy to create a sustainable energy system and decrease our dependence on fossil fuels. A balanced power grid system is the backbone of the electrified society, distributing electricity from renewable energy sources and powering our vehicles, industries, and electronics. Lithium-ion batteries are a key technology for both stationary and mobile energy storage and their optimal utilization should be carefully considered. Various degradation mechanisms contribute to performance fade in lithium-ion batteries. A key area of battery research is therefore to detect and characterize these mechanisms and predict their effects on battery performance. In this thesis, the performance of batteries is investigated in battery energy storage system (BESS) applications. The research questions cover different types of grid balancing services, methods to evaluate battery state of health (SOH) as well as the mechanisms causing the capacity and power fade. A combination of physics-based modelling and electrochemical techniques are applied, and the results combined to better understand the degradation and its consequences.

Frequency regulation, peak shaving, as well as a multi-service application are studied to evaluate battery performance and degradation stress factors and recommendations on operating conditions are developed. Cells with less than 65% of their nominal capacity are successfully utilized in a second application but evaluating SOH by the traditional methods is found to be insufficient. By updating electrochemical parameters in a physics-based model against data from the aged cells, sources of the performance loss are identified. This approach is further advanced as electrochemical impedance spectroscopy is used for parameter estimation. Cell degradation coupled to electrolyte consumption is highlighted. An improved SOH evaluation metric is suggested to explain the phenomenon of degradation resulting in uneven current distribution. This improved understanding of the internal cell degradation and *in situ* methods for quantitative evaluation will contribute to smarter utilization and longer battery lifetime.

## **Keywords**

Lithium-ion battery, degradation, stationary energy storage, electrochemical methods, physics-based modelling, parameter estimation, BESS, EIS, DVA, CDA



# Sammanfattning

Elektrifiering är vår mest lovande lösning för att skapa ett hållbart energisystem och minska vårt beroende av fossila bränslen. Ett välbalanserat elnät är ryggraden i det elektrifierade samhället, med elproduktion från förnybara energikällor som laddar våra fordon, industrier och elektronik. Litiumjonbatterier är en viktig teknik för både stationär och mobil energilagring och optimal användning bör nogra utvärderas. Prestationsförlust på grund av olika åldringsmekanismer är ett välkänt problem med litiumjonbatterier. Det är även utmaningen med att upptäcka och karakterisera dessa mekanismer, samt deras bidrag till prestationsförlusten. I denna avhandling studeras batteriers tillämpning i batterilagringssystem (BESS). Forskningsfrågorna inkluderar möjliga elnätsapplikationer, metoder för att utvärdera batterihälsa (SOH), samt mekanismerna som orsakar kapacitets- och effektförlust. Fysikbaserad modellering i kombination med elektrokemiska metoder tillämpas, och resultaten utvärderas för att bättre förstå batteriåldringen och dess konsekvenser.

Frekvensreglering, kapning av effekttoppar, samt en kombinerad tillämpning studeras, för att utvärdera batteriprestation och stressfaktorer för åldring. Rekommendationer för batteritillämpning och styrning utformas. Batterier med under 65% av den initiala kapaciteten kvar tillämpas även framgångsrikt i en "andra-applikation", men utvärderingen av SOH med traditionella metoder visas vara otillräcklig. Genom att uppdatera elektrokemiska parametrar i en fysikbaserad modell, mot data från de åldrade cellerna, identifieras källor till prestationsförlusterna. Denna metod blir vidare utvecklad då elektrokemisk impedansspektroskopi används för parameteruppskattning. Batteriåldring kopplad till elektrolytkonsumtion identifieras som en betydande faktor. Det gör även åldring som leder till ojämn strömfördelning i elektrodena och en förbättrad metod för utvärdering av SOH utifrån dessa faktorer presenteras. Med denna utvecklade förståelse för batteriåldring och *in situ* metoder för att kvantitativ utvärdering, kan batterier tillämpas smartare och livslängden förlängas.

## Nyckelord

Litiumjonbatteri, åldring, stationär energilagring, elektrokemiska metoder, fysikbaserad modellering, parameteruppskattning, BESS, EIS, DVA, CDA



## List of appended papers

- I. Mathilda Ohrelius, Magnus Berg, Rakel Wreland Lindström, and Göran Lindbergh. "Lifetime Limitations in Multi-Service Battery Energy Storage Systems." *Energies*, vol. 16, no. 7, 2023.
- II. Moritz Streb, Mathilda Ohrelius, Matilda Klett, and Göran Lindbergh. "Improving Li-ion battery parameter estimation by global optimal experiment design." *Journal of Energy Storage*, vol. 56, 2022.
- III. Moritz Streb, Mathilda Ohrelius, Aamer Siddiqui, Matilda Klett, and Göran Lindbergh. "Diagnosis and prognosis of battery degradation through re-evaluation and Gaussian process regression of electrochemical model parameters." *Journal of Power Sources*, vol. 588, 2023.
- IV. Mathilda Ohrelius, Rakel Wreland Lindström, and Göran Lindbergh. "Lithium-ion battery degradation in grid applications - analysis through frequency- and time-domain parameterization." Accepted by *Journal of The Electrochemical Society*.
- V. Mathilda Ohrelius, Rakel Wreland Lindström, and Göran Lindbergh. "Evaluation of simplified physics-based models in the frequency- and time-domain." Manuscript.
- VI. Mathilda Ohrelius, Göran Lindbergh, and Rakel Wreland Lindström. "Polarization effects and characterization of lithium-ion batteries for 2nd life applications." Manuscript.

Paper II and Paper III were collaborative studies and my contribution to the works will therefore be clarified. The studies include modelling work and design of experimental cycles based on sensitivity analysis. This was performed by M.S who also proposed the idea and developed the method. I performed the experimental work which included cycling the cells for parameterization and degradation, as well as opening cells and building half-cells for further characterization. I contributed to the writing in both articles as well as the degradation analysis in Paper III. In Papers I, IV, V and VI I did all the experimental and modelling work and analysed the results. I also wrote the first draft of the articles and incorporated input from the co-authors.



# CONTENTS

1	Introduction .....	5
1.1	Scope of the thesis .....	6
1.2	Background .....	8
1.2.1	The lithium-ion battery .....	8
1.2.2	Battery degradation.....	9
1.2.3	Physics-based modelling.....	12
1.2.4	Battery degradation in stationary energy storage.....	13
2	Materials and methods .....	15
2.1	Design of cycles .....	15
2.2	Cell types and chemistries.....	16
2.3	Electrochemical degradation analysis .....	17
2.3.1	Capacity .....	17
2.3.2	Differential voltage analysis .....	17
2.3.3	Electrochemical impedance spectroscopy.....	18
2.4	Physics-based modelling .....	18
2.4.1	Model parameters .....	18
2.4.2	Parameter estimation.....	23
2.4.3	Sensitivity analysis and optimal experiment design .....	24
2.4.4	Simplified modelling approaches .....	25
3	Results and discussion .....	27
3.1	Electrochemical degradation analysis .....	27
3.1.1	Capacity .....	27
3.1.2	Differential voltage analysis .....	31
3.1.3	Electrochemical impedance spectroscopy.....	33
3.1.4	Capacity difference analysis .....	36
3.2	Model based degradation analysis .....	40
3.2.1	Optimal cycles and parameter sensitivity.....	41
3.2.2	Parameterization in the frequency domain.....	42
3.2.3	Parameter re-evaluation with battery aging .....	44
4	Conclusions .....	51
	Outlook .....	53
	Acknowledgements .....	55
	References.....	56



# List of abbreviations

## Abbreviations

BESS	Battery energy storage system
BOL	Beginning of life (unaged)
BOT	Beginning of test (for cell previously cycled)
CC	Constant current
CDA	Capacity difference analysis
C-rate	Current normalized by cell capacity
CV	Constant voltage
DEC	Diethyl carbonate, $C_5H_{10}O_3$
DMC	Dimethyl carbonate, $C_3H_6O_3$
DVA	Differential voltage analysis
EC	Ethylene carbonate, $C_3H_4O_3$
EFC	Equivalent full cycle
EIS	Electrochemical impedance spectroscopy
EMC	Ethyl methyl carbonate, $C_4H_8O_3$
EOL	End of life
EOT	End of test
FEC	Fluoroethylene carbonate, $C_3H_3FO_3$
FR	Frequency regulation
HFR	High-frequency resistance
LAM	Loss of active material
LCO	Lithium cobalt oxide, $LiCoO_2$
LiB	Lithium-ion battery
LLI	Loss of (cyclable) lithium inventory
NCA	Lithium nickel cobalt aluminium oxide, $LiNi_xCo_yAl_{1-x-y}O_2$
NMC	Lithium nickel manganese cobalt oxide, $LiNi_xMn_yCo_{1-x-y}O_2$
NMP	N-methyl 2-pyrrolidone, $C_5H_9NO$
OCP	Open circuit potential
OCV	Open circuit voltage
P2D	Pseudo-two-dimensional
PS	Peak shaving
PV	Photovoltaic
RPT	Reference performance test
RUL	Remaining useful life
SCI	Self-consumption Increase

SEI	Solid electrolyte interphase
SEM	Scanning electron microscopy
SOC	State of charge
SOH	State of health
SOL	State of lithiation
SPM	Single particle model
VC	Vinylene carbonate, $C_3H_2O_3$

### Greek symbols

$\eta_{Li}$	Total available lithium content
$\eta_{s,+}$	Normalized total lithium content
$\Delta t$	Time constant
$\Phi$	Potential
$\alpha$	Charge transfer coefficient
$\varepsilon$	Volume fraction
$\eta$	Overpotential
$\kappa$	Electrolyte conductivity
$\tau$	Tortuosity

### Symbols

$i_0$	Exchange current density
$t_+$	Cationic transference number
Br	Bruggeman coefficient
$A$	Area
$C$	Capacitance
$D$	Diffusion coefficient
$F$	Faraday's constant
$J$	Flux of ions
$L$	Thickness
$Q$	Capacity
$R$	Resistance
$U$	Open circuit potential
$a$	Specific interfacial area
$c$	Concentration
$f$	Mean molar activity coefficient of an electrolyte
$i$	Current density
$k$	Reaction rate constant
$r$	Radius
$t$	Time
$v$	Electrode volume

### Sub- and super-scripts

±	Positive or negative electrode
cc	Current collector
dl	Double layer
host	Hosted
init	Initial
loc	Local
max	Maximum
min	Minimum
NE	Negative electrode
PE	Positive electrode
ref	Reference
sep	Separator
surf	Surface
<i>l</i>	Liquid phase (electrolyte)
<i>s</i>	Solid phase (active material)
<i>v</i>	Volumetric



# 1 Introduction

The reliance on energy in our society has drastically grown since the industrial revolution. New sources of energy have been unlocked and technological development has led to a vast increase in the amount of energy we consume. While human wealth and life quality has improved, challenges such as pollution and the overexploitation of resources have emerged as well. The power sector today accounts for the largest amount of greenhouse gas emissions (first and foremost CO<sub>2</sub>), followed by industry and transport [1]. To enable electrification of the transport sector as well as to protect energy security, lithium-ion batteries (LiBs) will play a crucial role [2]. Consequently, improvements in lithium-ion battery utilization will contribute to the UN sustainability goal 7 “Affordable and clean energy” as well as goal 11 “Sustainable cities and communities”.

Ambitious targets are declared worldwide to decrease our dependence on fossil fuels. At the COP28 UN Climate Change Conference in Dubai in 2023, nearly 200 countries agreed on the goal to triple the capacity of renewable energy by 2030 [3]. The power grid is the backbone of the green transition and to ensure reliable electricity supply a significant increase in electricity system flexibility is needed. Traditionally, the flexibility needed to meet variable power needs over time has been handled by ramping up the electricity produced by the power plants. As more intermittent energy sources are introduced, such as wind and solar power, new strategies are needed. The global capacity of battery energy storage systems (BESS) has increased exponentially in the last decade, from about 1 gigawatt in 2013 to over 85 gigawatts in 2023 [2] and the increasing trend is predicted to continue [4], [5], [6].

The development of the modern power grid system leads to new requirements for energy storage, possible business opportunities, and, as a result, a growing interest in different services BESS can provide. Since battery degradation is highly dependent on the utilization, BESS applications should be carefully considered and analysed before implementation. Three types of daily flexibility

services are often highlighted regarding BESS and commercially deployed. These are Frequency Regulation (FR), Peak Shaving (PS) and Self-consumption Increase (SCI) [7]. Different characteristics of the battery utilization in these services were identified by Kucevic et al. [7]. To ensure a stable grid frequency, FR needs to provide both charge and discharge power with a fast response time. This results in a highly dynamic utilization of the batteries and a large energy throughput. Using BESS as support during power peaks in PS results in a lower energy throughput, but longer periods of charge and discharge resulted in a wider voltage-window operation. For SCI, a photovoltaic (PV) unit was considered, resulting in dynamic charging as well as a more moderate voltage-window operation.

LiB degradation has been extensively studied over the years and the understanding of the degradation mechanisms, as well as the characterization techniques, are continuously improved [8], [9]. Material changes are often demonstrated by invasive methods harvesting the electrode sheets. A critical challenge remains when it comes to quantitatively correlate these changes to degradation of the battery performance. The new types of services introduced with BESS comprise another important area of research as great differences exist in battery utilization, compared to the more studied vehicle applications. More experimental studies analysing the degradation from realistic BESS services is therefore currently needed [10].

## 1.1 Scope of the thesis

This thesis aims to improve the understanding of lithium-ion battery degradation mechanisms, their effect on the battery performance, *in situ* evaluation methods of battery SOH and, from that, provide recommendations for their most beneficial use in stationary energy storage. Two types of commercial cylindrical batteries have been investigated. The first one is based on lithium nickel manganese cobalt oxide (NMC) as positive electrode and graphite as negative electrode (Paper I-V) while the second one is based on lithium nickel cobalt aluminium oxide (NCA) as positive electrode and graphite doped with silicon oxide as negative electrode, (Paper VI).

Different types of battery energy storage system (BESS) services were explored in Paper I. Three types of services were chosen to best cover possible degradation scenarios and a degradation study was performed on NMC cells. The electrochemical techniques differential voltage analysis (DVA) and electrochemical impedance spectroscopy (EIS) were applied to study the degradation phenomena as well as scanning electron microscopy (SEM). A more thorough degradation analysis was performed on NCA cells in Paper VI, as these cells were evaluated for repurposing in a 2<sup>nd</sup> application. The cells had previously been degraded to 60-65% of the nominal capacity. Capacity evolution trends for both 1<sup>st</sup> and 2<sup>nd</sup> application scenarios are studied and

capacity difference analysis (CDA) suggested as an addition to the SOH-evaluation metrics.

To monitor the batteries during operation, physics-based models allow not only for control over the cell voltage and current, but also provide detailed information about internal states and half-cell potentials. Some parameters needed in the model are determined by parameterization, which means finding the parameter values that result in the best fit of the model simulation to experimentally measured data (often voltage profiles). Optimal experimental design for improved parameter extraction is demonstrated in Paper II. The method results in the highest possible parameter sensitivity for the targeted parameter and gives improved confidence not only in a good fit to the data, but also in that the parameters are accurate in their physical description. The parameter-specific optimal experiments were further combined with the degradation study of the NMC cells (Paper I). By re-parameterizing the model with updated data as the cells degraded, degradation analysis was performed with a model-based approach in Paper III. Comparing the degradation results from the electrochemical analysis in Paper I with the parameter evolution in Paper III further supports the method of re-parameterization as a tool to evaluate battery degradation.

A tradeoff exists with physics-based battery models between complexity and computational speed. In Paper V we therefore investigated two simplified modelling approaches: one that is commonly applied (the Single Particle Model (SPM)) and one with a novel approach that we name the Electrolyte model. Both approaches were compared against the standard pseudo-2-dimensional (p2D) model. When validating against experimental EIS data both simplifications were found inaccurate and concluded insufficient, as the correct physical processes were not captured. Model re-parameterization from EIS data (with the p2D model) was explored in Paper IV. Additional service cycles were also designed and fresh as well as repurposed NMC cells degraded. Comparing the two different parameterization approaches (Paper III and IV) further advances the discussion on parameter accuracy, suitable experimental data, and parameter evolution with battery degradation. The main research questions summarizing this work are the following:

- How can BESS be operated in the best way in terms of delivered energy and battery lifetime?
- How can the battery state of health be properly evaluated?
- What are the sources of the performance fade?

## 1.2 Background

### 1.2.1 The lithium-ion battery

LiBs deliver electricity as the negative electrode releases one electron and one lithium ion and  $\text{Li}^+$  migrate from the negative to the positive electrode through the electrolyte. The porous electrodes are usually coated on current collector foils as a slurry consisting of active material, conductive filler, and binder. During battery operation, the electrochemical reaction is distributed over the surface of the active material particles and will vary throughout the depth of the electrode, see Figure 1. Key developments have included the storage of lithium in the electrodes through intercalation (improving the reversibility), finding electrode materials with a large electrochemical potential difference (graphite-based negative electrodes and transition metal oxide-based positive electrodes) and developing stable electrolytes with fast mass transport properties. The 2019 Nobel Prize in Chemistry was awarded to Whittingham, Goodenough and Yoshino for their work in meeting these challenges [11]. Lithium cobalt oxide (LCO) is the original positive electrode chemistry and has been used for over three decades. With cobalt listed as a critical material (essential to energy technologies but having a high risk for supply chain disruption), the trend in the industry is to exchange the cobalt with other elements. Higher energy densities have been achieved with lithium nickel manganese cobalt oxide (NMC) and lithium nickel cobalt aluminium oxide (NCA). Generally, higher nickel content gives higher energy density but the material instability at high potential increases as well [12]. Negative electrodes are almost exclusively based on graphite due to its high capacity, good rate-performance, and low electrode potential. Due to its possibility to significantly increase the energy density in LiBs, silicon is considered a suitable substitute for graphite. However the larger volume change of Si during lithium intercalation is a challenge for its long-term stability [13]. The electrolyte consists of liquid organic solutions in a mixture of linear (e.g., dimethyl carbonate (DMC), ethyl methyl carbonate (EMC), and diethyl carbonate (DEC)) and cyclic (e.g., ethylene carbonate (EC)) carbonates as solvents and commonly lithium hexafluorophosphate ( $\text{LiPF}_6$ ) as the conducting salt [14]. In commercial cells, common additives include fluoroethylene carbonate (FEC) and vinylene carbonate (VC) for improving the stability of the solid electrolyte interphase (SEI) layer.

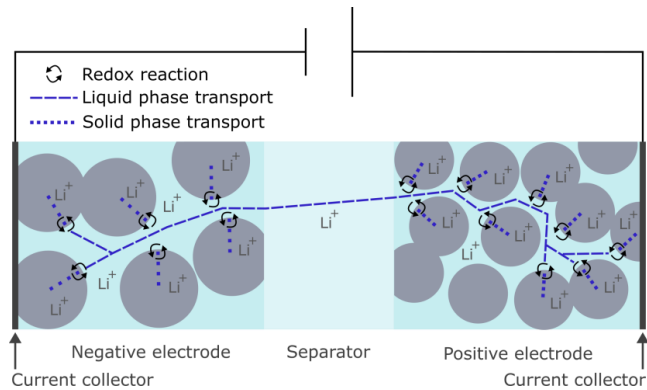


Figure 1: Illustration of a lithium-ion cell showing the solid phase (active material particles; the conductive filler and binder are not shown), the solution phase (electrolyte), and the interfaces where the electron transfers occur. Potential drop and concentration changes in both the solid and the solution phases will lead to a distribution of current density through the depth of the porous electrodes.

### 1.2.2 Battery degradation

The amount of power and energy a battery can deliver decreases over its lifetime as a result of mechanical, chemical, and electrochemical processes. Battery degradation is often analysed at three different levels. At the lowest level, the actual mechanisms responsible for the performance decay are studied. These are often grouped into observable consequences at cell level, called degradation modes. The degradation modes include loss of active material at the positive or negative electrode (LAM<sub>PE/NE</sub>), loss of cyclable lithium inventory (LLI), and impedance increase. At the highest level, the operational effects are evaluated, i.e., the capacity and power fade. In this work, we take a slightly different approach when studying the degradation mechanisms and their effects. Since electrochemical techniques are combined with physics-based modelling, additional information is obtained about the performance degradation in terms of mass transport characteristics (in the solid and liquid phase), as well as reaction kinetics within the two electrodes. We refer to this level of battery degradation analysis as performance-based. It is more detailed than degradation modes analysis and does not reveal responsible mechanisms per se, but rather reveals their effects on the battery processes during operation. The three main dynamic processes are shown in Figure 2, as well as degradation mechanisms that can impact the performance.

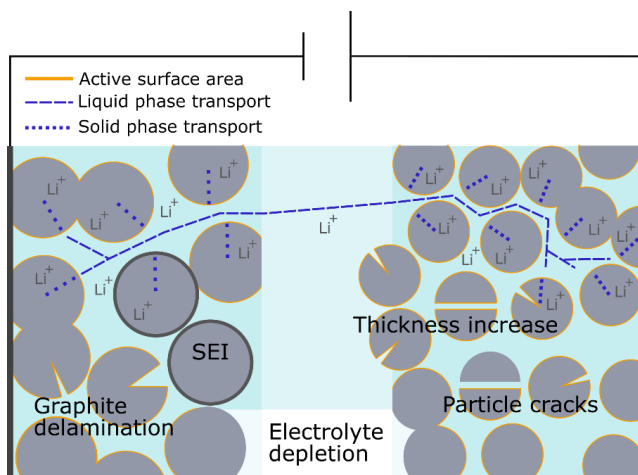


Figure 2: Illustration of the performance-based degradation analysis. Degradation mechanisms observed in this work are shown and coupled to the three main dynamic processes in battery operation. The redox reaction happening at the interface between the solid and liquid phase is illustrated as the active surface area, as these are connected.

The main degradation mechanism reported in literature is the solid electrolyte interphase (SEI)-layer growth. The low potential of the negative electrode will drive the electrolyte to react at its surface, creating a Li-containing interphase layer. Initially, up to 10% of the first-cycle capacity can be lost due to the loss of cyclable lithium inventory (LLI), but as the fresh electrode surface gets covered with SEI, this reaction slows down [9]. Slower lithium transport through the SEI can result in an impedance increase, or even effectively block the redox reaction from happening, as illustrated in Figure 2. The liquid-phase transport might also be affected for two reasons. The first is that as the SEI layer grows, it might clog pores and/or make them more narrow, causing a more tortuous path for transport. The second is that the mass transport properties of the electrolyte may deteriorate as solvent components are consumed and the composition changes.

Degradation mechanisms of the active material in the electrodes include structural changes, decomposition, or particle fractures [9]. Particle fracture, resulting from material stress due to the (de)intercalation of lithium, can have both beneficial and detrimental consequences for battery performance. If new pore space is created and filled with electrolyte, improved kinetics might be observed as the active surface area will increase. This would on the other hand also lead to increased SEI-layer growth. Cracks could also improve the mass transport in the solid phase if the diffusion length gets shortened. If particles crack and segments become isolated, LAM will instead decrease the available capacity (and active surface area). While the volume changes due to lithium intercalation are mainly reversible, permanent deformation is sometimes

observed [15] and can result in decreased tortuosity, illustrated as an electrode thickness increase in Figure 2.

Lithium plating is another mechanism that can be detrimental to battery lifetime and safety and, furthermore, can be also challenging to identify [16]. It can be exacerbated by low temperatures, high state of charge (SOC), and high currents and results in metallic lithium plating on the negative electrode and/or the separator. The reaction can be both reversible and irreversible.

Lastly, inhomogeneous degradation in the cells is becoming more relevant as the battery performance increases and the cells are utilized longer [16], [17], [18]. Uneven current distribution due to, for example, surface layers on the electrodes, further accelerates the degradation mechanisms. Another possibility is electrolyte degradation, resulting in locally decreased mass transport properties and, in extreme cases, even electrolyte depletion. While it is known that the SEI-layer growth consumes electrolyte, the transport properties are often still assumed to remain constant during the life of a battery. Electrolyte degradation as a cause of power and capacity fade has been highlighted in recent studies [18], [19], [20].

#### **1.2.2.1 Electrochemical methods**

Remarkable progress has been made when it comes to understanding and identifying degradation mechanisms and improving battery cell design over the years. However, battery degradation cannot be completely avoided, and as the power and energy needs are being pushed, so too are the batteries. Developing better tools and methods to go beyond *ex situ* and local degradation characterization is therefore a topic of active research, both from the viewpoint of electrochemistry as well as from the viewpoint of operation and control. To quantify how different mechanisms contribute to full cell performance includes challenges of both spatial and temporal resolution. In addition, only information about voltage, current and sometimes temperature is available during normal operation. To tackle this problem of limited information and resolution, several advanced and creative methods have been developed through the electrochemical understanding of battery operation. In the following two of these methods will be further explained.

Early work of differential voltage analysis (DVA, often also called  $dV/dQ$ ) was performed by Bloom et al. [21], [22], to separate electrode information from full cell data. Subtle plateaus and slope changes in the electrode open circuit potential (OCP) behaviour can easier be distinguished and tracked as the voltage data is differentiated with respect to the capacity. A low-current full-cell charge or discharge is often used in the analysis to obtain the pseudo-open circuit voltage (pOCV). In the differentiated data, peaks and flatter regions often appear which can be separated for each electrode. The origin of these features stem from structural changes in the host matrix of the electrode (phase transformations) as the concentration of intercalated lithium

changes. When two or more phases exist in equilibria (having the same lithium chemical potential) voltage plateaus appear, referred to as phase equilibria. Between two plateaus, one phase will dominate and the voltage change in this region is due to this phase transition (seen as a peak in the DVA). The electrode health can then be further evaluated through tracking the distance between the observed peaks in DVA and the capacity obtained between these phase transitions. In this way, DVA is used to identify the sources of capacity loss, i.e. the degradation modes  $LAM_{PE/NE}$  and LLI.

Electrochemical impedance spectroscopy (EIS) is another valuable tool to evaluate the impedance of the cells, affecting the power performance. As a small perturbation signal (voltage or current) is applied over a range of frequencies, the impedance contributions can be decoupled and further assigned to different processes in the cell. The data is often visualized in a Nyquist diagram, with the imaginary part of the impedance on the y-axis, and the real part on the x-axis with one point plotted per measured frequency. Capacitive behaviour can stem from the redox reactions and the charging of the double layer, or from  $Li^+$  conduction through electrode surface layers. At lower frequencies, the diffusion processes are rate-limiting and often appear as a “diffusion tail”, similar to the case of diffusion in a semi-infinite domain [23]. EIS is widely applied to evaluate battery performance in both academia and industry [24] but with a great amount of information the correct interpretation of the data also becomes more challenging. Equivalent circuit models are often used to fit the data and further decouple the impedance contributions. The problem is that many different circuits containing different elements may produce a good fit and that a direct relation to the fundamental physicochemical processes is lacking. In this thesis, EIS is fitted to a physics-based p2D model to decouple and understand the impedance contributions.

### **1.2.3 Physics-based modelling**

Physics-based battery models are built on first-principles physical descriptions of batteries, including transport laws and rate expressions, formulated within the continuum hypothesis. While high accuracy can be achieved, the computational cost and complexity is a challenge. An efficient approach is to reduce the dimensions that are resolved for, where possible. The pseudo-2-dimensional or p2D model (developed by Fuller, Doyle and Newman [25]) is commonly used as a tradeoff between complexity and solver speed. It considers a 1D cross-sectional slice containing two porous electrodes separated by a separator and a pseudo particle dimension for lithium intercalation.

#### **1.2.3.1 Degradation modelling**

In addition to the electrochemical techniques applied to evaluate battery SOH, a wide range of modelling approaches are available as well. SEI-layer growth is

often modelled as a reaction between EC and lithium ions, limited either by the kinetics or diffusion of solvent through the SEI [26]. Lithium plating can be modelled in a similar way assuming standard Butler-Volmer or Tafel kinetics [26]. Stress models considering the particle expansion during lithiation have also been developed. This can lead to layer/particle cracks resulting in fresh exposed active surface area and increased LLI and LAM [26]. A critical problem raised in the review and model performance comparison by Reniers et al. is that many different models can be fitted to a small experimental data set [26]. Hence, a good fit of a degradation model to experimental data does not automatically prove that the correct degradation physics have been modelled. Another problem highlighted by Edge et al. [9] is that the interplay between mechanisms is often ignored. It is well known that different degradation mechanisms will occur simultaneously and that they can both accelerate and decelerate each other, as was proficiently demonstrated in the review of the “aging knee” phenomenon [27]. The inclusion of such interplay in the degradation models will drastically increase the computational cost, as well as drive a need for new experimental methods to enable correct model parameterization.

A different approach to capture degradation effects with a model is to re-evaluate the model parameters and compare the simulation with experimental data as the cells degrade. If the model is physics-based, changes of the parameter values can be coupled to internal changes in the cell. Two main advantages exist with this approach. The first is fewer parameters to be determined, as including additional degradation physics would necessitate more unknown parameters. The second advantage is that the degradation is not assumed beforehand (as when designing the degradation model), which might give misleading or biased results.

#### **1.2.4 Battery degradation in stationary energy storage**

To design service cycles suitable for experimental studies, Dubarry et al. analyzed three years of BESS operation data and created representative duty cycles based on five design factors [28]. Three of these were selected as main stress factors for battery degradation; C-rate, temperature, and SOC swing range, of which temperature was found to have the biggest impact on the degradation rate [29]. Different positive electrode chemistries have also been studied in BESS applications. A lower capacity loss rate was observed for LiFePO<sub>4</sub> (LFP) compared to Ni-rich electrodes when cycled in a wide SOC window [30], [31]. Kim et al. found the degradation rate for three types of Ni-rich electrodes to be initially higher than LFP, but after a year decreased to a similar rate [32]. Degradation modes from BESS applications were further analysed through incremental capacity analysis [33].

BESS with batteries retired from vehicle applications have been successfully demonstrated for different services ([34], [35]) and the first European EV

battery 2<sup>nd</sup> life system was implemented in 2014 by BMW [36]. Great potential was shown in a study by Gao et al. using batteries from a Nissan Leaf Gen 1 with under 67% remaining pack capacity [37]. By restricting the operating conditions, the degradation rate could be more than halved compared to their 1<sup>st</sup> life. More studies are needed to fully understand battery degradation in 2<sup>nd</sup> applications and determine how to best evaluate battery SOH.

## 2 Materials and methods

### 2.1 Design of cycles

Five different cycling protocols were designed to study degradation of BESS. The mildest service was frequency regulation (FR), which consists of shallow pulses around 50% SOC and a maximum C-rate of 1 (FR<sub>1C</sub>) or 1.5 (FR<sub>1.5</sub>). Here, C-rate is the applied current divided by the cell capacity, hence 1C-rate is the current applied for a discharge in 1 h. The FR-cycle was taken from data published by Sandia National Laboratories in their report “Protocol for Uniformly Measuring and Expressing the Performance of Energy Storage Systems” [38]. It is representative of a 2 h FR service and the data is scaled to be cycled galvanostatically. Peak shaving (PS) requires operation in a wider SOC window and consists of longer periods of constant current charge and discharge followed by periods of rest. To study the effect of the current amplitude, two C-rates were applied for PS as well: PS<sub>1C</sub> and PS<sub>0.5C</sub>. With their differences in power and energy needs, combining two or more services might be a viable strategy for BESS operation. The combination of FR<sub>1C</sub> and PS<sub>1C</sub> was therefore also studied in Paper I, referred to as FRPS<sub>2C</sub>. The duty cycles are shown in Figure 3. Cycled cells were kept in a climate chamber at 40°C to accelerate the rate of the degradation. Four additional calendar aging tests have also been conducted. At 40°C, three different SOC levels were included, 22%, 50% and 78%, referred to SOC<sub>22</sub>, SOC<sub>50</sub> and SOC<sub>78</sub> from now on. At 25°C, a reference test at 50% SOC was included, referred to as SOC<sub>50</sub><sub>25°C</sub>.

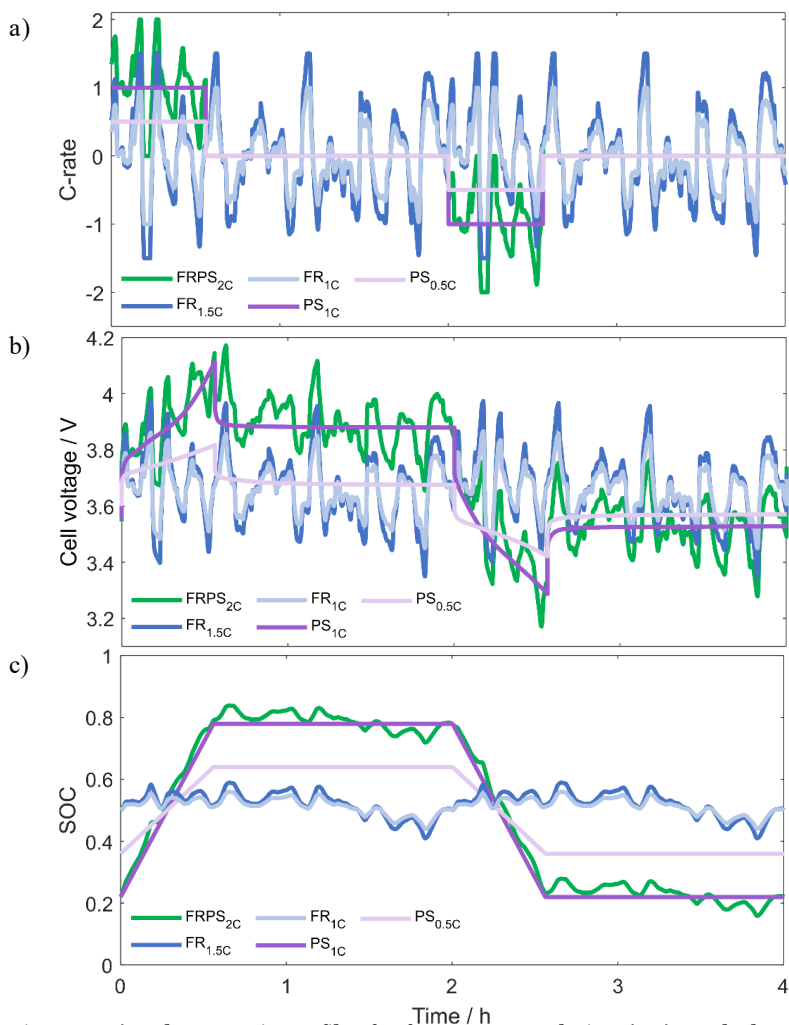


Figure 3: a) Galvanostatic profiles for frequency regulation (FR), peak shaving (PS), and the combined cycle (FRPS) with the maximum C-rate in the subscript. b) Measured voltage response from the galvanostatic profiles at beginning of life for the NMC/Gr cells. c) State-of-charge (SOC) intervals for the galvanostatic cycles. The cycles are symmetric, and the initial cell voltage determined for an average SOC of 50%. Adapted from Paper IV.

## 2.2 Cell types and chemistries

The cells studied in this thesis are two types of commercial lithium-ion battery cells. One cell type has  $\text{LiNi}_{0.5}\text{Mn}_{0.3}\text{Co}_{0.2}\text{O}_2$  (NMC532) as positive electrode active material and graphite (Gr) as negative electrode. It is a cylindrical 18650 type cell with a nominal capacity of 2.6 Ah, it will be referred to as NMC/Gr.

The other cell type has  $\text{LiNi}_{0.9}\text{Co}_{0.05}\text{Al}_{0.05}\text{O}_2$  (NCA) as positive electrode and Gr + silicon oxide ( $\text{SiO}_x$ ) as negative electrode. It is a slightly larger cylindrical 21700 type cell with a nominal capacity of 4.6 Ah and will be referred to as NCA/Gr- $\text{SiO}_x$ . These cells are only studied in Paper VI and evaluated for a 2<sup>nd</sup> application utilization. They were previously cycled in a different study [39].

Electrode sheets were harvested from the commercial cells to rebuild cells in a three-electrode setup (EL-CELL, ECC-PAT-core) with a lithium reference electrode. The coating on one side of the electrodes was first removed through a combination of swabbing with solvents and scraping. The solvents used were N-methyl- 2-pyrrolidone (NMP) and dimethyl carbonate (DMC). With the current collector exposed on one side, circular electrodes were then prepared by punching the sheets. The electrodes, 100  $\mu\text{L}$  electrolyte (1 M LiPF<sub>6</sub> in 1:1 EC:DEC vol., BASF Selectilyte® LP40), and the reference electrode were then reassembled in the three-electrode setup.

## 2.3 Electrochemical degradation analysis

The cell degradation was paused every second week to perform reference performance tests. The batteries were let to rest for two hours at 25°C before measurements of capacity and impedance were conducted.

### 2.3.1 Capacity

The standard procedure for the capacity measurements was a C/2-rate constant-current (CC) charge to the maximum cell voltage, followed by a constant-voltage (CV) hold until the current dropped below C/20. First, a 1C-rate discharge capacity was measured (defined from the nominal capacity), followed by a C/20-rate capacity measurement (updated from the actual 1C capacity). The available capacity of the cell depends on several factors. (1) the charging strategy before the measurement affects how much lithium gets intercalated in the negative electrode, (2) cell polarization influences the discharging capability at higher currents, as well as (3) ambient temperature. In Paper VI we explore different charging and discharging strategies to get as close as possible to the thermodynamic properties of heavily degraded cells. We then vary the CC and CV conditions, as well as the rest period between the charge and the discharge.

### 2.3.2 Differential voltage analysis

C/20-rate discharge data was initially used for the DVA (Paper I), while in Paper VI we analyse the effect of different current amplitudes. To obtain distinguishable peaks, the smoothing approach as suggested by Li et al. [40] and Smith et al. [41] was applied. This approach includes a pre-processing of the raw data by smoothing with a moving average over a 0.1% SOC span, followed by a Gaussian filter with a 3.0% SOC span.

### 2.3.3 Electrochemical impedance spectroscopy

EIS was measured after a CCCV charge to 50% SOC (defined by Coulomb counting), followed by 3 h rest. Galvanostatic impedance was performed with a current perturbation of 260 mA and a frequency range of 50 mHz-3000 Hz, using a four-point connection cell holder.

## 2.4 Physics-based modelling

The modelling work in this thesis has all been based on the p2D model. In Papers II and III the modelling work was performed by a collaborator and solved with Python Battery Mathematical Modelling (PyBaMM). In Papers IV and V the modelling was performed in COMSOL Multiphysics. As different parameterization strategies have been applied, these will be further explained below. Results are presented later.

### 2.4.1 Model parameters

For accurate simulations with the p2D model, cell specific parameters need to be determined. Some, such as geometric parameters, can be measured by opening a reference cell and harvesting the electrode sheets. Parameters related to the electrolyte mass transport properties are often taken from the literature. Finally, some parameters are highly cell-specific and need to be determined by fitting the model to experimental data (i.e. parameterization). The focus in this thesis has been on the last subset of parameters determined through parameterization. The targeted parameters in the different studies are shown in Table 1 and will be further explained in the following chapters. The additional parameters needed for the p2D model are explained in Table 2.

Table 1: Dynamic and thermodynamic model parameters determined through different parameterization approaches in this thesis.

Parameter	Description	Paper II	Paper III	Paper IV
$\tau_{\pm} / Br_{\pm}$	Tortuosity	o	o	o
$\Delta t_{\pm} / D_{\pm}$	Intercalation diffusivity	o	o	o
$k_{\pm}$	Kinetic rate constant	o	o	o
$R_{SEI}$	SEI layer resistance	(o)		
$R_{cc}$	Current collector resistance		o	o
$\varepsilon_{l,\pm}$	Electrode porosity	(o)		
Balancing		o	o	o
$D_l$	Electrolyte diffusivity			o
$\kappa$	Electrolyte conductivity			o
$C_{dl,\pm}$	Double layer capacitance			o

Table 2: Additional p2D model parameters not directly estimated in the thesis.

Symbol	Description
$\sigma_{s,\pm}$	Electrical conductivity
$t_+$	Cationic transference number
$f$	Mean molar activity coefficient
$c_{l,init}$	Initial electrolyte Li <sup>+</sup> concentration
$\alpha_{a,\pm}, \alpha_{c,\pm}$	Anodic/cathodic charge transfer coefficient
$U_{\pm}$	Open circuit potential (OCP)
$L_{\pm}$	Electrode thickness
$\varepsilon_{sep}$	Separator porosity
$L_{sep}$	Separator thickness

#### 2.4.1.1 Thermodynamic parameters

A strategy when performing parameterization of the model is to decrease the interactions of other unknown parameters where possible. A common approach is therefore to start with the parameters related to the cell thermodynamics and fit them to experimental data at, or close to, open circuit conditions. A full cell discharge at C/20-rate can be used, assuming that the processes causing cell polarization can be reasonably neglected. This parameterization step is called electrode balancing, as it determines the relationship between the full cell state of charge (SOC) and the electrode state of lithiation ( $SOL_{\pm}$ ). Most electrodes that host lithium by intercalation present different characteristics in their potential curve as the lithium concentration changes. These features are visible when looking at the OCP vs.  $SOL$ , or when measuring the potential at a very low charge/discharge current i.e. pseudo-OCP (pOCP). The pOCP for both electrodes are measured experimentally and defined as  $U_{\pm} = f(SOL_{\pm})$  in the model. For a correct electrode balancing, the maximum and minimum  $SOL$  need to be determined for both electrodes, see an example in Figure 4. The four parameters ( $SOL_{max/min,\pm}$ ) are then used to calculate the initial lithium concentration from the initial SOC ( $SOC_0$ ) and the maximum concentration of Li<sup>+</sup> in the electrodes ( $c_{max,\pm}$ ) from:

$$c_{init,+} = SOL_{max,+} - SOC_0(SOL_{max,+} - SOL_{min,+})c_{max,+} \quad (2.1)$$

$$c_{init,-} = SOL_{min,-} + SOC_0(SOL_{max,-} - SOL_{min,-})c_{max,-} \quad (2.2)$$

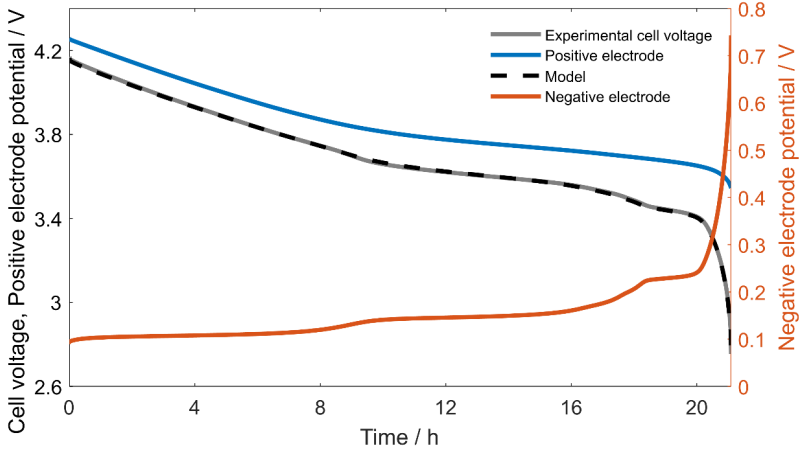


Figure 4: Illustration of the electrode balancing parameterization step where  $SOL_{\max/\min,\pm}$  is determined from a low current discharge. The open circuit voltage is defined as  $U_{\pm} = f(SOL_{\pm})$ , where  $SOL_{\pm} = c_{\text{surf},\pm}/c_{\text{max},\pm}$ .

As well as the electrode active material volume fractions, calculated from:

$$\varepsilon_{s,\pm} = \frac{Q_{\text{cell}}}{F c_{\text{max},\pm} A_{\text{cell}} L_{\pm} (SOL_{\text{max},\pm} - SOL_{\text{min},\pm})} \quad (2.3)$$

Where  $A_{\text{cell}}$  is the electrode area and  $L_{\pm}$  the thickness of the electrode.  $Q_{\text{cell}}$  is a parameter manually updated as the measured C/20 capacity for each experiment.

A different balancing approach was implemented in Paper II and III. Rather than fitting  $SOL_{\max/\min,\pm}$ ,  $\varepsilon_{s,\pm}$  was directly fitted, as well as a normalized amount of cyclable lithium:

$$\eta_{s,+} = \frac{\eta_{\text{Li}}}{Q_{\text{host},+}} \quad (2.4)$$

The electrode host capacity can be calculated from:

$$Q_{\text{host},\pm} = c_{\text{max},\pm} v_{\pm} F \quad (2.5)$$

Where the total volume of active material is:

$$v_{\pm} = A_{\text{cell}} L_{\pm} \varepsilon_{s,\pm} \quad (2.6)$$

And the total available lithium content:

$$n_{Li} = SOL_+ Q_{host,+} + SOL_- Q_{host,-} \quad (2.7)$$

The different parameterization approaches will be discussed further in the Result and discussion section.

#### 2.4.1.2 Dynamic parameters

As soon as a current is applied the lithium in the battery will start to move and the current-dependent dynamic battery behaviour appears. In the porous electrode, lithium moves between a solid phase (the active material) and a liquid phase (pores filled with electrolyte). The solid phase transport is modelled as a diffusive process, where the active material particles are assumed perfectly spherical and homogeneous. The relaxation and polarization behaviour are described by Fick's law:

$$\frac{\partial c_s}{\partial t} = \nabla \cdot (D_{\pm} \nabla c_s) \quad (2.8)$$

Where  $c_s$  is the concentration of lithium in the particle and the solid phase diffusivity  $D_{\pm}$  is determined through parameterization. The boundary condition at the particle surface for the local charge-transfer current density ( $i_{loc}$ ) is:

$$D_{\pm} \left. \frac{\partial c_s}{\partial r} \right|_{r = r_{surf}} = - \frac{i_{loc}}{F} \quad (2.9)$$

The diffusion time is coupled to the diffusion length, i.e. the particle radius, through:

$$\Delta t_{\pm} = \frac{r_{\pm}^2}{D_{\pm}} \quad (2.10)$$

In the liquid phase the transport of ions is modelled through the concentrated solution theory. Properties of interest are the electrolyte salt diffusivity ( $D_l$ ), electrolyte conductivity ( $\kappa$ ), transference number ( $t_+$ ) and the thermodynamic factor (calculated from the mean molar activity coefficient,  $f$ ). Studies measuring these intrinsic ionic transport properties can be found [42], [43], but as the cell degrades and different constituents of the electrolyte are consumed by side reactions, over time these properties will change. In Paper

IV, the evolution of  $D_l$  and  $\kappa$  with cell degradation is investigated, while in Paper III they are assumed constant.

In porous media, the transport path length is further dependent on the tortuosity ( $\tau$ ). Low tortuosity values indicate a straighter path, whereas a higher tortuosity means a more obstructed and longer path for the ions to travel. To account for this in a simplified 1D simulation, a scaling factor is used, resulting in an effective diffusivity and conductivity according to:

$$D_{l,eff} = \frac{\varepsilon_l}{\tau} D_l, \quad \kappa_{eff} = \frac{\varepsilon_l}{\tau} \kappa, \quad \tau = \varepsilon_s^{1-Br} \quad (2.11)$$

Where  $\varepsilon_l$  is the electrolyte volume fraction and Br is the Bruggeman coefficient. The mass balance in the liquid phase is expressed as:

$$\frac{\partial \varepsilon_l c_l}{\partial t} + \nabla \cdot \mathbf{J}_l = \frac{A_v i_{loc}}{F} \quad (2.12)$$

Where  $c_l$  is the concentration of lithium in the electrolyte,  $A_v$  is the specific surface area and  $\mathbf{J}_l$  is the electrolyte flux of  $\text{Li}^+$  calculated from:

$$\mathbf{J}_l = -D_l \nabla c_l + \frac{i_l t_+}{F} \quad (2.13)$$

Where  $i_l$  is the current density in the solution phase and  $t_+$  is the transference number. The charge balance equation in the liquid phase is:

$$\nabla \cdot i_l = A_v i_{loc} \quad (2.14)$$

And the electrolyte current density is expressed as:

$$i_l = -\kappa_{eff} \nabla \Phi_l + \frac{2\kappa_{eff} RT}{F} \left( 1 + \frac{\partial \ln f}{\partial \ln c_l} \right) (1 - t_+) \nabla \ln c_l \quad (2.15)$$

Where  $\Phi_l$  is the electric potential in the electrolyte and  $f$  the mean molar activity coefficient of the electrolyte.

The final property of interest is the rate of lithium moving between the solid and liquid phase. This flux at the particle surface is driven by the electrochemical reaction and modelled by the Butler-Volmer equation

$$i_{loc} = i_0 \left\{ \exp\left(\frac{\alpha F \eta}{RT}\right) - \exp\left(\frac{-\alpha F \eta}{RT}\right) \right\} \quad (2.16)$$

Where  $\alpha$  is the charge transfer coefficient ( $\alpha_a = \alpha_c = 0.5$  assumed),  $i_0$  is the exchange current density i.e. the value of oxidation and reduction currents

when the electrode is at rest and  $\eta$  is the surface overpotential. The former can be expressed through a reaction rate constant  $k$  (here including electrolyte concentration) and a concentration dependence as:

$$i_0 = F\hat{k}c_{\text{surf}}^\alpha(c_{\text{max}} - c_{\text{surf}})^\alpha \left( \frac{c_l}{c_{l,\text{ref}}} \right)^\alpha \quad (2.17)$$

$$k_\pm = \hat{k}_\pm F / \sqrt{c_{l,0}} \quad (2.18)$$

Where  $c_{\text{surf}}$  is the concentration of lithium at the particle surface.

To simulate the battery impedance response, double-layer capacitances on the active electrode materials was added and the current through the double layer calculated as:

$$i_{\text{dl}} = i\omega(\Phi_s - \Phi_l)C_{\text{dl}} \quad (2.19)$$

Where  $\Phi_s$  is the solid phase potential,  $\omega$  the angular frequency and  $C_{\text{dl}}$  the double layer capacitance.

#### 2.4.2 Parameter estimation

Parameter estimation by fitting the physics-based model to experimental data can be an efficient and non-intrusive method, but initialisation and validation is a challenge. There are three fundamental parts of an optimization problem: the control variables (parameters of interest, or fitting parameters), the objective function, and additional constraints. The objective function can be formulated as a least-square type, evaluating the sum of squared differences between the experimental data and the model output. Solving the optimization problem then means to find the value of the control variables that minimizes the objective function.

A variety of optimization solvers exist to solve the minimization problem. While finding the optimal solver was not the focus in this work, the main challenges and differences will be briefly explained. The two main groups of optimization solver algorithms are the gradient-based solvers and the derivative-free solvers. The gradient-based solver follows a path where each new iterate is based on the local derivative evaluated at previously visited points. While this can provide advantages in solver speed, problems often occur when the objective function is non-smooth or contains noise. Battery models are nonlinear and the objective function often non-convex. It is then a risk of the solver “getting stuck” finding only a local minimum and not the global one. Derivative-free solvers, on the other hand, rely on sampling the objective function at different positions in the control variable space. This is more expensive than following a single path toward the optimum but also

more robust. It can improve the likelihood to find the global minimum, but this is not guaranteed. Selecting suitable initial values when fitting several control parameters at once is crucial independent of the type of solver, especially when considering the complex interplay of the processes in lithium-ion batteries. In Paper IV, two different optimization solvers were utilized for parameter fitting in COMSOL. For the frequency domain simulation, the gradient-based SNOPT solver was used, while the gradient-free Nelder-Mead solver was used in the time domain.

### **2.4.3 Sensitivity analysis and optimal experiment design**

Parameter sensitivity analysis and the development of optimal experiments for parameterization was performed in Paper II. The study was continued in Paper III and the results lead to the idea for Paper V. The concept and development of the methodology in Paper II was performed by a collaborator and will therefore only be explained briefly here.

The importance of sensitivity analysis stems from the fact that the quality of a fit (simulated voltage vs. experimentally measured voltage) is not automatically equivalent to quality of parameters. The solution for the optimization problem will converge if the solver finds some trend where changing the control variables results in a decrease of the objective function, down to a defined value. Changing one parameter might lead to a large effect on the simulated output (high sensitivity), while another parameter results in a small change i.e. the parameter has a low sensitivity under those circumstances. A risk with parameters having low sensitivity is that processes are included in the model that have very little or no impact on the simulation output, i.e. the model gets overparameterized. It can also be the case that a parameter has low sensitivity in one situation, for example during low current operation, but very high sensitivity as the current increases. This was explored in Paper II. Eight parameter specific experiments were designed with the criteria of the highest possible sensitivity towards that parameter, using three design factors: current amplitude, dynamics and state of charge (SOC). The global sensitivity analysis is based on Sobol's method, in which the variance contribution from each parameter is deconvoluted from the total observable variance. An optimality criterion is defined to maximize the influence of the targeted parameter in that experiment, as well as to minimize the interdependence and concurrent sensitivity of the other parameters. The optimization problem was then iteratively solved through a Bayesian optimization method with a maximum of 40 iterations (i.e. the number of designed and evaluated optimal experiments). The final result was eight different current trajectories, one for each parameter, with the highest possible sensitivity toward the desired parameter.

#### 2.4.4 Simplified modelling approaches

Based on the results from the parameter sensitivity analysis in Paper II, as well as another study by Streb et al. [44], the diffusion coefficients in both the positive and negative electrodes ( $D_{\pm}$ ) were found to have a low sensitivity during normal battery operation conditions. Interestingly, the electrolyte diffusivity  $D_l$  was found to have a high sensitivity. This led us to explore two approaches for simplified physics-based battery models in Paper V. First, the commonly applied single particle model (SPM) was evaluated, assuming negligible effects of the electrolyte dynamics when operating at a maximum C-rate of 1C [45]. Instead, the SPM assumes the intercalation diffusion ( $D_{\pm}$ ) to be the rate limiting process and ignores the effects of  $D_l$ . Second, as the opposite to the SPM, a model called the Electrolyte model was developed. It considers the mass transport in the electrolyte and  $D_l$  to be the rate limiting process, while it ignores the polarization due to the diffusion in the particles.

The evaluation of the models was performed in three steps. As the parameterization of the p2D model had been previously performed in Paper IV, these results were used as initial values. In step 1, the polarization contributions from the processes were assumed negligible (intercalation diffusion or electrolyte diffusion) and thus were simply removed to see the effect on the simulated output. In a second step, the simplified models were reparameterized against time-domain experimental data. Finally, in a third step, the obtained parameters were evaluated in the frequency domain for validation. As only the diffusion processes were compared in the frequency-domain validation (EIS), the p2D model was used for all simulations and only the diffusivities varied.



## 3 Results and discussion

### 3.1 Electrochemical degradation analysis

#### 3.1.1 Capacity

##### 3.1.1.1 1<sup>st</sup> application

To evaluate how different types of operation affect the cells, their capacity is often studied either vs. time or vs. equivalent full cycles (EFC), where 1 EFC is equivalent to the energy throughput needed for one complete charge and discharge of the cell. It is useful to compare the degradation that occurs due to different working conditions. Different degradation behaviors occur when the cell is at rest, i.e., calendar aging, or if a current is applied, i.e., cycle aging. The capacity loss due to calendar and cycle aging of the NMC/Gr cells are evaluated in Figure 5. All cells had a duplicate and the average value with error bars indicating the range in the observed values is shown. As the cells were cycled at 40°C to decrease the experimental time needed, two reference cells were also calendar aged at 50% SOC and 25°C (SOC50<sub>25°C</sub>). These low-temperature cells, as expected, showed the lowest rate of capacity loss. LiBs with a graphite-based negative electrode are known to have capacity loss driven by the negative electrode potential [46]. A lower negative electrode potential increases the rate of SEI-layer growth, i.e., at a high cell voltage. The same trend is seen here as SOC78 has the highest rate of capacity loss, followed by SOC50 and SOC22 (calendar aged cells). The PS-cycled cells, while showing a similar rate of degradation loss between the duplicates, had a large gap between them. For visibility, the main panel of Figure 5 shows only the average value of PS<sub>1C</sub> and PS<sub>0.5C</sub>, while the difference is plotted in the inset.

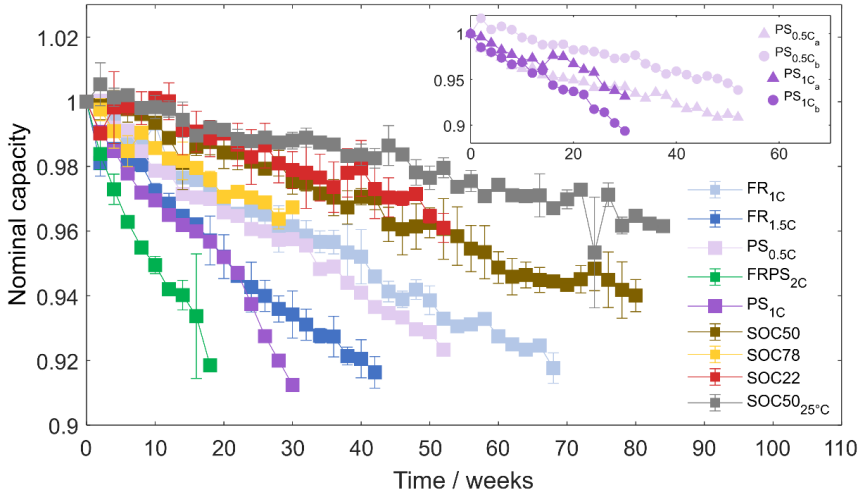


Figure 5: Capacity evolution of the calendar- and cycle-aged NMC/Gr cells. The data shows the averaged value of duplicate cells with error bars for all cells except for  $PS_{1C}$  and  $PS_{0.5C}$ , which are plotted individually in the inset. Reproduced from Paper I but with the addition of  $FR_{1.5C}$ ,  $PS_{0.5C}$  and  $SOC_{22}$ .

For the cycle-aged cells, the fastest capacity loss is seen for the combined cycle  $FRPS_{2C}$ , which could be expected as the current is increased and thereby the rate of charge throughput.  $PS_{0.5C}$  has the lowest rate of charge throughput, 25 EFC between each reference performance test (RPT), but still shows a slightly higher rate of capacity loss than  $FR_{1C}$  (66 EFC/RPT measurement). The longer periods of charge and discharge, resulting in a larger  $\Delta SOC$  (and more time at high SOC), seem to stress the cells more than the charge throughput.  $FR_{1C}$ , performing shallow pulses around 50% SOC, accelerates the capacity loss rate by 60% compared to pure calendar aging at 50% SOC.  $FR_{1.5C}$  and  $PS_{1C}$  initially show a similar degradation rate, but an increase is observed for  $PS_{1C}$  after 20 weeks. This could be an indication of a change of the dominant degradation mechanism. A similar trend can be seen for  $FRPS_{2C}$  after 14 weeks of operation.

To get a better picture of the cycle aging related to the working conditions, the capacity evolution vs. EFC is plotted in Figure 6. Two clear rates of capacity loss are seen for the five different cells. A slower trend for FR and a faster rate for PS and FRPS. When increasing the maximum current for the mildest cycle  $FR_{1C}$  by 50% to  $FR_{1.5C}$  and decreasing the maximum current for  $PS_{1C}$  by 50% in  $PS_{0.5C}$ , a greater spread in the capacity loss rate was expected. The voltage response of the galvanostatic cycles at beginning of life (BOL) are displayed in Figure 3b. Although the charge pulses in  $FR_{1.5C}$  results in a higher voltage than  $PS_{0.5C}$ , the rate of capacity loss still follows  $FR_{1C}$ , and  $PS_{0.5C}$  follows  $PS_{1C}$  and  $FRPS_{2C}$  for the duration of the experiment. This indicates that something other than the voltage or current amplitude is driving the capacity loss.

An explanation can be found in the SOC profiles, calculated from the galvanostatic cycles, in Figure 3c. The cell voltage is the result of the open circuit voltage (OCV) plus the polarization. The OCV variation, resulting from the amount of lithium stored in the electrodes (and SOC), is lower for FR<sub>1.5C</sub> than PS<sub>0.5C</sub>, although the cell voltage is higher. As the SOC exceeds 60%, the lithiation of the negative electrode will reach a new stage level (the ordering of intercalated lithium in the host structure), causing additional mechanical stress to the graphite particles. This has been shown before to have a correlation with capacity loss rate [46].

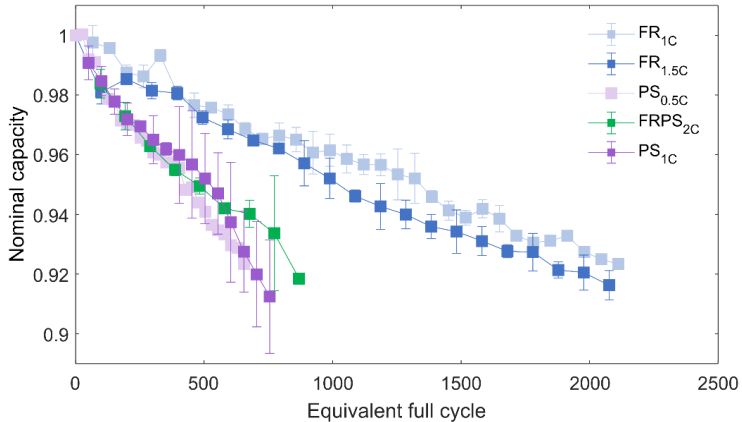


Figure 6: Capacity evolution of the cycle-aged NMC/Gr cells vs. equivalent full cycle. Adapted from Paper IV.

### 3.1.1.2 2<sup>nd</sup> application

To study cells repurposed for a 2<sup>nd</sup> application, results for both the NMC/Gr cells and the NCA/Gr-SiO<sub>x</sub> cells will be discussed.

For the NMC/Gr cells the data from both the 1<sup>st</sup> and the 2<sup>nd</sup> application is shown in Figure 7 (Paper IV). Here the cell name refers to the 1<sup>st</sup> application performed and the 2<sup>nd</sup> application is FR<sub>1.5C</sub> for all cells. When changing the application to the milder FR<sub>1.5C</sub> cycle (filled markers) the PS<sub>1C</sub> shows a decreasing capacity loss rate, similar to the purely FR<sub>1.5C</sub>-cycled cells. For FRPS<sub>2C</sub>, the first eight RPTs show a slower capacity loss rate, followed by a steeper drop. This shows that changing the application of previously degraded cells, in this case narrowing the operating voltage window, can slow down the degradation rate and prolong the lifetime of the cells. However, the faster capacity loss rate of FRPS<sub>2C</sub> compared to PS<sub>1.5C</sub> in the 2<sup>nd</sup> application indicates that the history of the cells has an impact and necessitates thorough characterization.

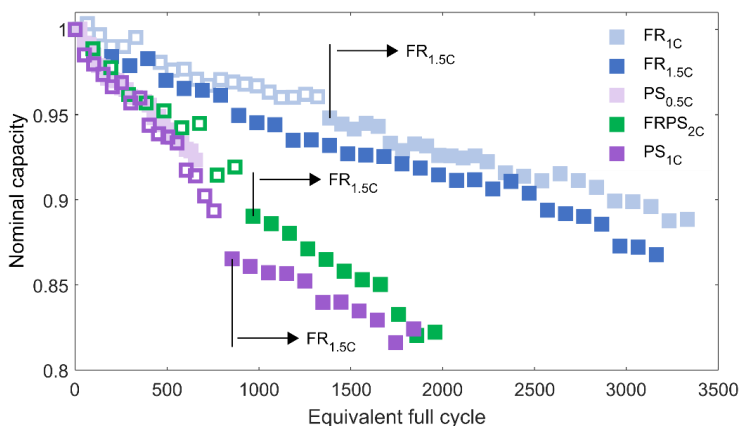


Figure 7: Capacity evolution of the NMC/Gr cells for both 1<sup>st</sup> and 2<sup>nd</sup> applications. The stage where the cells have been repurposed to perform FR<sub>1.5C</sub> is marked. Adapted from Paper IV.

Previously degraded NCA/Gr-SiOx cells were picked to study strategies for battery SOH evaluation and the suitability of new applications (Paper VI). The goal was to find methods to evaluate the battery SOH without prior knowledge of their history. Four cells were selected and matched to duplicate cells with a similar capacity and impedance to evaluate their 2<sup>nd</sup> application performance. Two different cycling protocols were applied to study the suitability of the service types. Cell C and Cell B were repurposed for the milder FR application due to the lower capacity at the beginning of test (BOT). As a reference, Cell A and Cell B were cycled at a 1C-rate (3 A) between 20-80% SOC, i.e. constant-current (CC) cycling. The capacity evolution of the cells is shown in Figure 8. The capacity was measured at the initial C/20-rate i.e. -0.15 A for Cell A/B and -0.138 A for Cell C/D and the current was not further adjusted throughout the test, hence, the polarization contribution to the capacity measurement will increase with time. Although picking cells with similar EIS and DVA responses, a spread in the capacity evolution from the same type of cycling is still observed. To understand and be able to predict the fast capacity loss rate for Cell A is especially important before 2<sup>nd</sup> application utilization. Additional techniques will be applied to understand this behaviour.

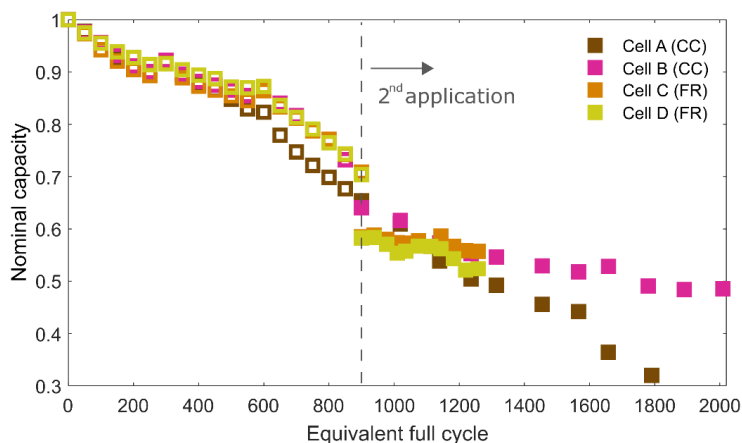


Figure 8: Capacity evolution of the NCA/Gr-SiO<sub>x</sub> cells for both 1<sup>st</sup> and 2<sup>nd</sup> application. 1<sup>st</sup> application data from [39] and 2<sup>nd</sup> from Paper VI. Adapted from Paper VI.

### 3.1.2 Differential voltage analysis

#### 3.1.2.1 NMC/Gr cells

To analyze the degradation modes of the NMC/Gr cells, DVA was conducted with the C/20-rate discharge data measured at every RPT. By differentiating the voltage with respect to the capacity ( $dV/dQ$ ), electrode-specific features can more easily be distinguished. In Paper I, a reference three-electrode setup measurement was performed to identify the peak contributions from each electrode, as shown in Figure 9a. The negative electrode shows flat regions in the DVA, as well as two clear peaks. A voltage plateau during the discharge results in a DVA value of zero as  $\Delta V=0$ . On the other hand, peaks in the DVA can occur if  $\Delta V$  at some point increases and is followed by a decrease, i.e., the peak stems from the steepest point. These peaks originate from phase transitions in the electrodes due to the lithium (de)intercalation. If active material is lost, the capacity obtained between these peaks will decrease and the distance between the peaks (as  $dV/dQ$  is plotted vs.  $Q$ ) will shrink. The result for FRPS<sub>2C</sub> during 18 weeks of operation is shown in Figure 9b. It is concluded that no LAM<sub>NE</sub> occurs as the distance between the two graphite peaks stays constant. No clear peaks from the positive electrode are visible and the analysis therefore relies on other features in the curve. After the second graphite peak, at around 2.25 Ah discharged capacity, the DVA drops before the last increase at the end of the curve. It was discussed in Paper I that this depth was controlled by the positive electrode and a decreased depth is an indication of LAM<sub>PE</sub>. In a recent paper by Sieg et al. [47], it is demonstrated how electrolyte depletion also can contribute to a similar shift. Without clear peaks from the positive electrode, it therefore cannot be determined whether LAM<sub>PE</sub> or electrolyte depletion is the reason for this behaviour.

Finally, inhomogeneous degradation is observed as the peaks get smeared out with time. This could also be an effect of electrolyte depletion, or the formation of surface layers that block  $\text{Li}^+$  transport and result in a distribution in the state of lithiation (SOL) between the particles. The discussion of degradation modes will be continued in Chapter 3.2.3 and particularly in the section about thermodynamic parameters, where the parameterization results from the electrode balancing are presented.

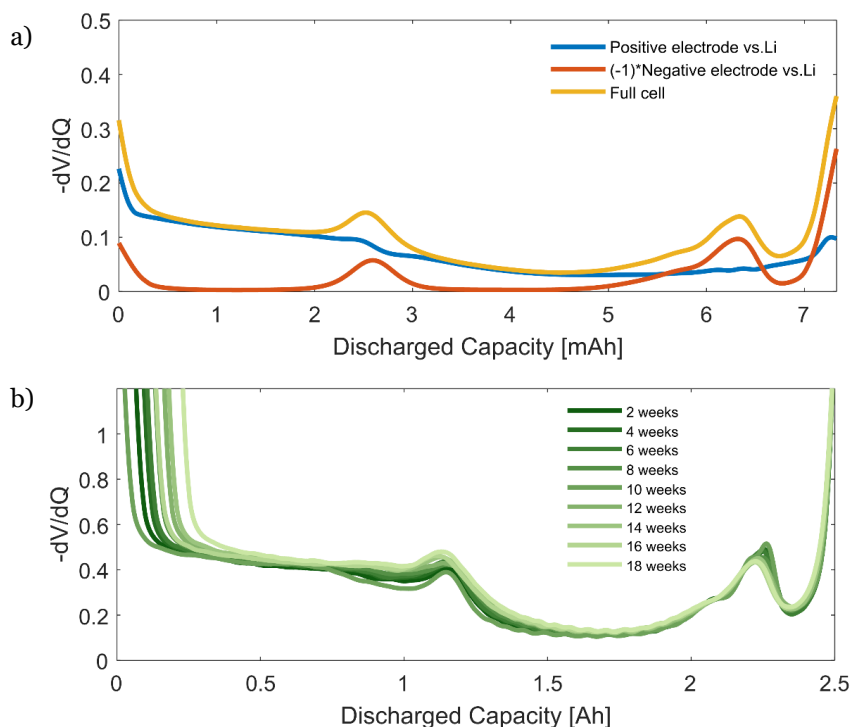


Figure 9: Differential voltage analysis of the NMC/Gr cells. a) Data measured in a three-electrode setup with a lithium reference electrode. b) Data measured for a cell performing FRPS<sub>2C</sub>. The plots are centred at the end of the discharge for a better comparison of the negative electrode peaks. Reproduced from Paper I.

### 3.1.2.2 NCA/Gr-SiO<sub>x</sub> cells

DVA for the NCA/Gr-SiO<sub>x</sub> cells concluded LAM<sub>PE</sub> and LAM<sub>NE</sub> for Cell A and B, as the distance between the peaks decreased, but not for Cell C and D, in Paper VI. Furthermore, the shift of the first peak in the discharge (P1) to the left on the x-axis (see Figure 10a) commonly ascribed to LLI was shown to be highly affected by the polarization during the charging step before the measurement. When plotting  $dV/dQ$  vs.  $Q$  in Figure 10a a clear shift of P1 is seen for the aged cells, compared to the unaged BOL cell. When plotting the

same data but vs. the cell voltage ( $dV/dQ$  vs. V) in Figure 10b the shift is instead observed at the start of the discharge, i.e. the initial cell voltage. As the cells begin from different voltage points after the charging procedure (even with a stop current condition of C/100 during the CV step), the initial cell SOC affects the peak positions in the DVA. The shift of the peak can therefore not be regarded as simply an electrode shift and LLI, but the polarization at high SOC must be accounted for as well. Regardless, a shift does still occur, as N1 appears before P1 for Cells A and B and seems to be merged with P1 for Cells C and D. New tools to decouple thermodynamic losses such as LLI from polarization effects therefore need to be further developed.

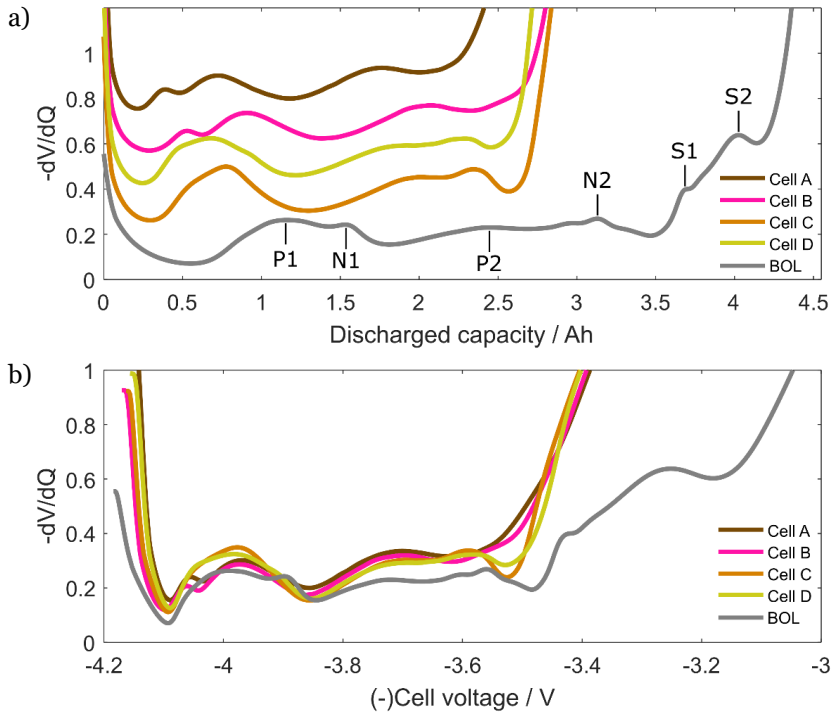


Figure 10: Differential voltage analysis ( $dV/dQ$ ) for the NCA/Gr-SiO<sub>x</sub> cells, plotted vs. the discharged capacity Q in a) and vs. the cell voltage V in b). Peaks are assigned according to [48] and the discharge current is C/100 rate. In a) the lines are plotted with an offset in the y-direction for better visibility. Adapted from Paper VI.

### 3.1.3 Electrochemical impedance spectroscopy

Different processes in LiBs have different rates. One way to describe these processes is by their characteristic time, that is the time required for a process to return to steady state after an applied perturbation. In EIS measurements, the frequency variations of the applied signal allow the deconvolution of

processes according to their respective characteristic times. Electron transfer and ion conduction in the electrolyte is often assigned to the lowest characteristic times, while diffusion typically has the highest (slowest processes). Since some processes also show a capacitive behaviour, the EIS result is often visualised through a Nyquist diagram, with the imaginary part of the impedance on the y-axis and the real part on the x-axis.

### **3.1.3.1 NMC/Gr cells**

In Paper IV we begin by visually inspecting the EIS data, followed by fitting the data to a p2D model for further parameter extraction. The impedance evolution of PS<sub>1C</sub> and PS<sub>0.5</sub> are shown in Figure 11 a-b. Two values extracted from EIS are tracked and plotted vs. capacity in Figure 11c-d for all cycle-aged cells in the study. These are the intercept of the plot with the x-axis, referred to as the “high-frequency resistance” (HFR) and the local minimum marking the width of the semicircle (marked with the triangle). The HFR is determined by the fastest processes in the cell: the ion conduction in the electrolyte and the transport of electrons through current collectors and between connections in the circuit. The semicircle represents the combined impedance from the transport of ions through the porous electrodes and the charge transfer reactions. While PS<sub>1C</sub> and PS<sub>0.5C</sub> showed a similar capacity loss rate in Figure 6, the impedance evolution shows different trends. All cells experience a linear rate of HFR increase with capacity loss as seen in Figure 11c. A similar growth of the semicircle is seen for PS<sub>1C</sub> and FRPS<sub>2C</sub> (Figure 11d), but not for PS<sub>0.5C</sub>, FR<sub>1C</sub> or FR<sub>1.5C</sub>. For the latter case the width of the semicircle remains rather constant, highlighting differences in the degradation mechanisms. The similar trends in the HFR increase indicate that electrolyte degradation is not connected to the semicircle growth. Instead, kinetic limitations are believed to be the source. Changes of the electrode surface, layer growth and/or decreased active surface area are all reported degradation mechanisms [9].

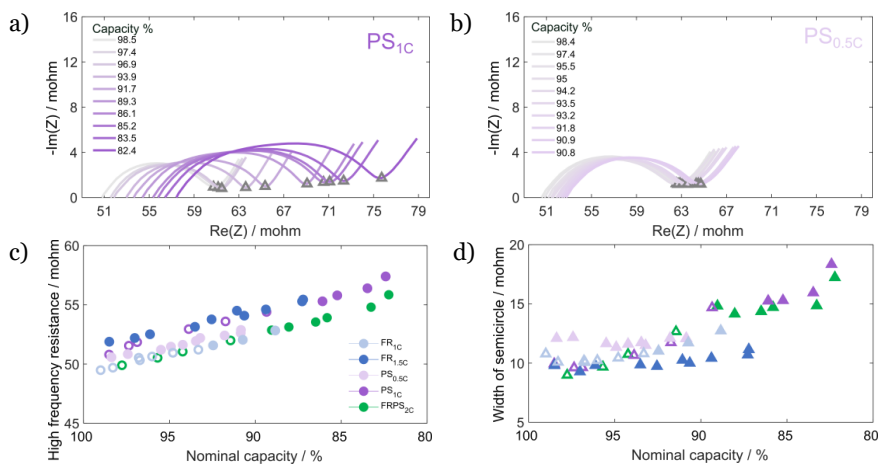


Figure 11: Electrochemical impedance spectroscopy of the NMC/Gr cells. The impedance evolution with capacity for a)  $PS_{1C}$  and b)  $PS_{0.5C}$ . c) The high-frequency resistance (x-axis intercept) with capacity evolution for all cycle-aged cells. d) The width of the semicircle for all cycle-aged cells. Adapted from Paper IV.

### 3.1.3.2 NCA/Gr-SiO<sub>x</sub>

The impedance evolution of the NCA/Gr-SiO<sub>x</sub> cells in their 2<sup>nd</sup> application is shown in Figure 12. The previously degraded cells were picked to have a similar initial impedance at BOT. Two depressed semicircles are shown initially for all cells and as the cells degrade both semicircles grow. Cell A experiences the largest impedance increase, both with the HFR and the semicircles, followed in turn by Cells B, D and C. The local minimum, including the impedance from electron transfer, mass transport in the electrolyte and charge transfer kinetics, is tracked (marked with a star) and will be further discussed when deconvoluting polarization in the next chapter.

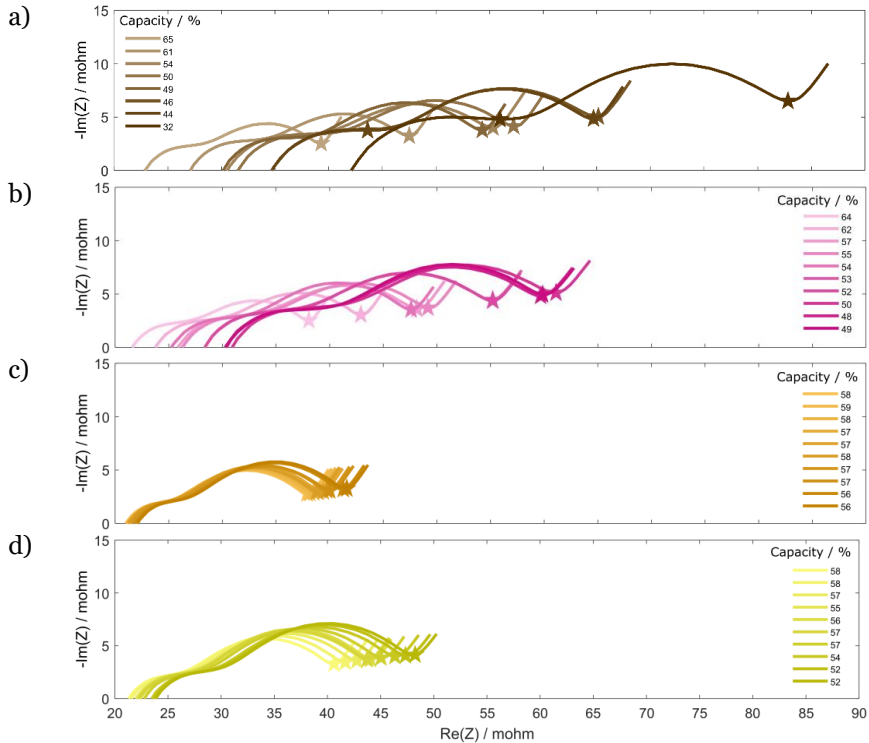


Figure 12: Impedance evolution of the NCA/Gr-SiO<sub>x</sub> cells measured at 50% SOC. a) Cell A (CC), b) Cell B (CC), c) Cell C (FR), d) Cell D (FR). The star marks the local minima which for Cell A and B slows down from 0.24 Hz BOT to 0.19 Hz and for Cell C and D stays constant at 0.24 Hz. Adapted from Paper VI.

### 3.1.4 Capacity difference analysis

In Paper VI, we identified the need for further characterization beyond capacity and impedance to evaluate the battery SOH and predict the remaining useful life (RUL). The capacity measurement, followed by DVA, measures a full discharge at a low current to get as close to the thermodynamic properties as possible, i.e., to be able to neglect polarization. EIS on the other hand is performed at steady state, to neglect the impact of electrode thermodynamics, and instead identify and deconvolute the sources of polarization. During longer periods of discharge, as more of the Li<sup>+</sup> is utilized, polarization due to mass transport limitations can become more important. Compared to EIS, in which only a small amount of charge is involved, a full battery discharge includes complete delithiation of the negative electrode, transport of all the Li<sup>+</sup> in the electrolyte (through the porous electrodes and the separator) and further intercalation in the positive electrode. This leads to a buildup of concentration gradients in both the solid and liquid phases.

Capacity difference analysis (CDA) is a way to quantitatively evaluate this polarization effect. Introduced by Lewerenz et al. [49], CDA includes the comparison of the discharged capacity at a low current with a higher current. Interesting phenomena can be observed with this method at different stages in the life of a battery. At BOL, similar to the results presented in [49], we see an evolution of decreasing CDA for all cycle-aged NMC/Gr cells, in Figure 13. This can be explained by an overdimensioned negative electrode (also called anode overhang), designed to avoid lithium plating. The overhang refers to the design where no positive electrode is positioned opposite to this region and a lateral flow of lithium in the negative electrode therefore is introduced. The mass transport of lithium in the solid phase is known to be a rather slow process and while the lower C-rate discharge also measures the capacity stored in the overhang, the discharge at the higher current is too fast, and the capacity remains unutilized. The decrease in CDA as initially seen in Figure 13 can be explained by a loss of contact with the overhang area, due to a higher current density at the edge, resulting in cracks, or electrolyte dry out [49].

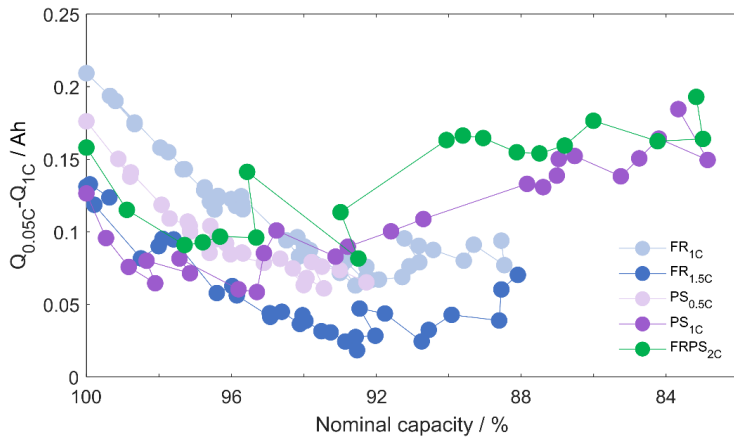


Figure 13: The capacity difference evolution of the cycle-aged NMC/Gr cells.

An increase in the CDA is later observed for the cells in Figure 13, as well as for the more heavily degraded NCA/Gr-SiO<sub>x</sub> cells in Figure 14e. Increasing CDA results from a higher rate of polarization increase, compared to the rate of capacity loss. This can be seen in Figure 14a-d, where the voltage profiles for the 0.05C-rate and 1C-rate discharge data is shown over the cycle-aging period, discharged capacity is shown on the x-axis. Cell A quickly reaches a point of power limitations, where almost no capacity is obtained from the 1C discharge. Interestingly, Cell B shows a similar polarization increase when looking at the impedance evolution, in Figure 14f, but does not show the same behaviour in the CDA. It might therefore include an explanation to the fast degradation rate of Cell A compared to Cell B, when performing the same CC service.

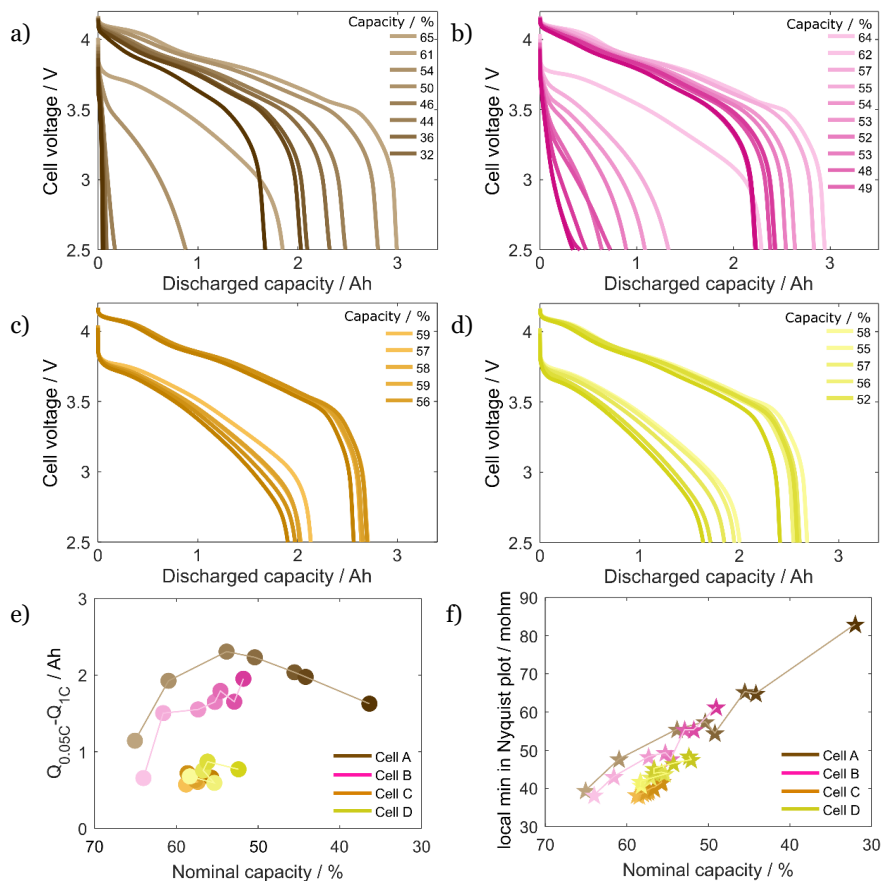


Figure 14: Discharge profiles for the four NCA/Gr-SiO<sub>x</sub> cells at 0.05C- and 1C-rate during the cycle study. a) Cell A (CC) b) Cell B (CC) c) Cell C (FR) d) Cell D (FR) e) The capacity difference (CDA) obtained from the data in a-d. f) The impedance evolution, start marked in Figure 12. Adapted from Paper VI.

To better understand the source of this capacity difference, the capacity was additionally measured at several C-rates and analysed through DVA, in Figure 15. The unaged BOL cell (Figure 15c) does not show any shift of the peaks when increasing the C-rate, but only a steeper slope at the end of the discharge resulting in slightly less available capacity. Cells A and B however show a different behaviour, in Figure 15a-b. For the degraded cells, a higher C-rate results in a decreasing distance between the peaks. This “LAM” as previously discussed when comparing DVA at different battery SOH, now shows unutilized active material (power limitations) as different current amplitudes are compared (rather than the comparison of batteries at different degrees of

degradation). We believe this behaviour originates from mass transport limitations and see two possible scenarios. In the first scenario, mass transport limitations introduce a lateral flow of lithium (in a similar way as the anode overhang introduced it at BOL). If the lithium transport through the separator is blocked, due to separator damage or electrolyte dry out, this slower lateral transport will be introduced in the electrode [16]. With faster discharge rates (higher currents), fewer ions will have time to reach the areas where the separator is not blocked, and therefore ions stored in the electrode become unutilized. The second scenario is presented from our results in Paper IV, where we re-evaluated parameters in the p2D model for aged cells. In the study, a decreased electrolyte diffusivity was found to have a strong impact on the battery response for longer periods of charge and discharge but was not visible in the impedance response. Electrolyte solvents are known to be consumed due to SEI-layer growth, and this is likely to affect the mass transport properties as well.

Finally, comparing Cells A and B in Figure 15a-b, the effect of unutilized electrode capacity with higher currents is much more prominent for Cell A, where the 1C-rate discharge is not even visible. This can therefore explain the higher CDA for Cell A, as the peak distance decrease correlates well with the lower measured capacity.

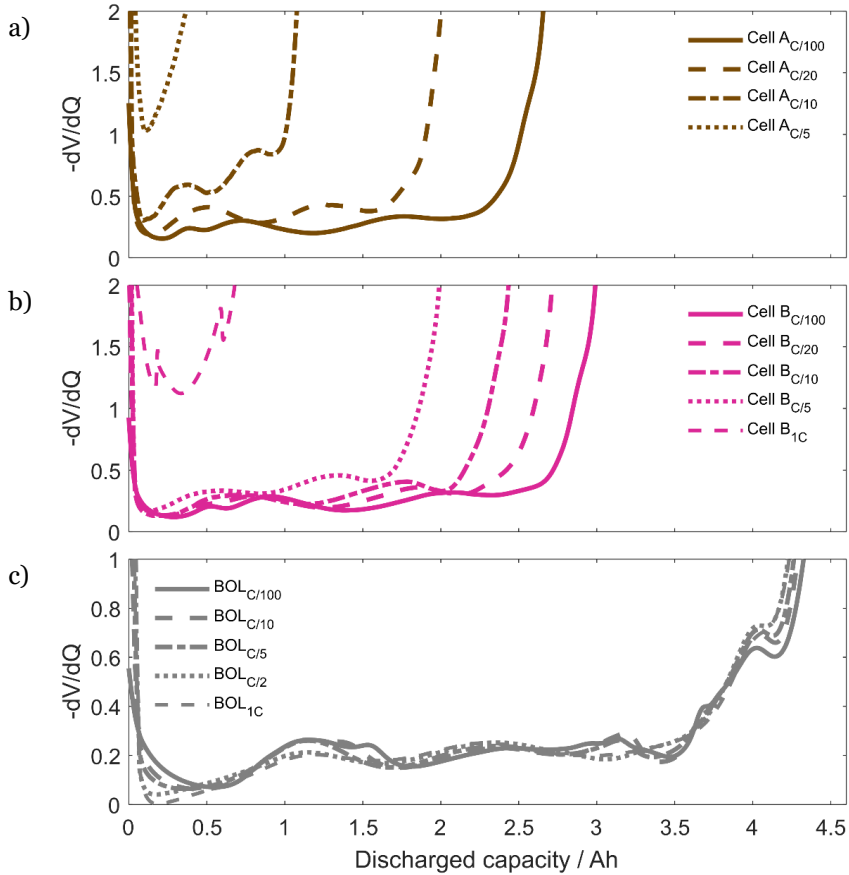


Figure 15: Differential voltage analysis of the NCA/Gr-SiO<sub>x</sub> cells at different C-rates. The aged cells A and B in a-b) show unutilized active material for higher currents (peak distance decrease), while the unaged cell in c) shows no peak shift with higher currents. Adapted from Paper VI.

### 3.2 Model based degradation analysis

The following results are based on the NMC/Gr cells only. The results presented in this chapter start with the parameter sensitivity analysis performed in Paper II and the design of optimal experiments for parameterization (in the time domain). This is followed by the results from parameterization with impedance data (frequency domain) in Paper IV and the evaluation of the two simplified physics-based models in Paper V. Finally the degradation analysis through re-evaluation of the parameters will be presented (Paper III and Paper IV) and compared with the electrochemical degradation analysis in Paper I.

### 3.2.1 Optimal cycles and parameter sensitivity

A parameterization strategy improving the parameter quality and simulation accuracy was demonstrated in Paper II. Overall, the parameters obtained from the optimal experiments improved the model performance by at least 40% over three different validation sets when compared to parameterization from a 1C-discharge curve. The improvement mainly results from better simulation of the fast dynamic response.

As discussed when studying the impedance, as different processes exhibit different characteristic times, we also expect different dynamics in the optimal experiments. This is observed in Figure 16a, where processes with a small characteristic time, such as the charge transfer reactions (and their reaction rates,  $k_{\pm}$ ), demand very dynamic cycles as their optimal experiments. These are clearly different from the processes with a larger characteristic time such as diffusion, where the optimal experiment for  $D_{+}$  comprises a simple constant-current discharge at high SOC. It should be noted here that the experiments for  $k_{+}$  and  $k_{-}$  turned out to be very similar in terms of their design factors: current amplitude, dynamics, and SOC. This indicates that separating the contributions from each electrode might be difficult from full cell data.

Another observation is that while  $D_{+}$  has the highest sensitivity at the highest SOC, effectively resolving  $D_{-}$  requires a profile at the lowest SOC. One of the most popular simplifications of the p2D model is the SPM, where the effect of the electrolyte dynamics is neglected and solid-phase diffusion is assumed to be the limiting process. The results here indicate that this might not be the case in the majority of the operating voltage range, i.e., the medium SOC region. The data for parameterization was measured during a battery charge and the resulting voltage profile including all experiments is shown in Figure 16b.

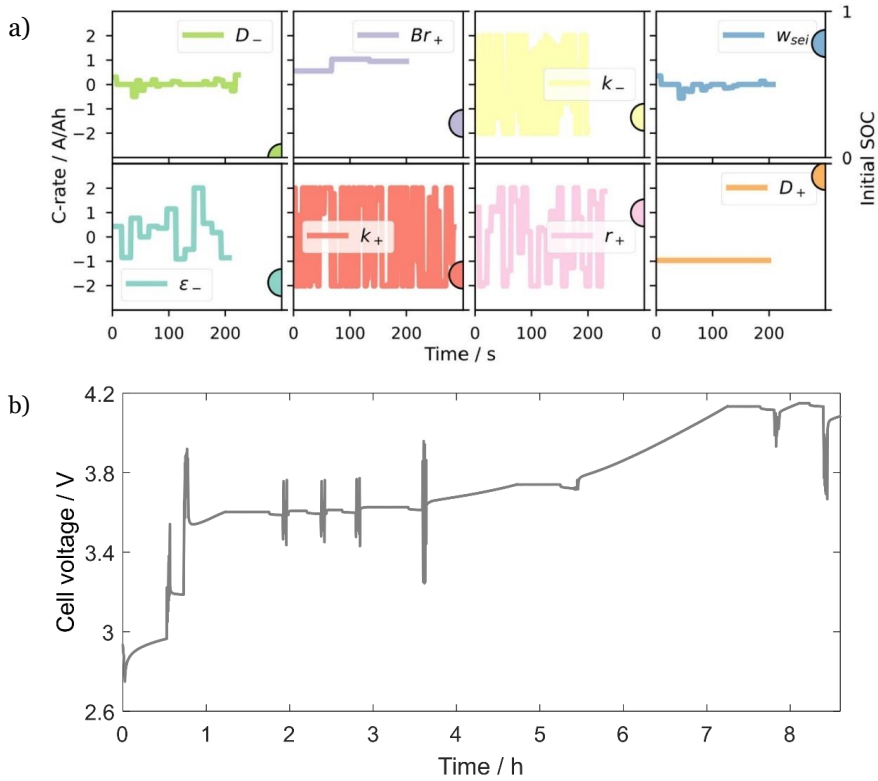


Figure 16: a) Current trajectories and initial state of charge obtained from the parameter specific optimal experiments, reproduced from Paper II. The targeted parameters are the electrode diffusivities ( $D_{\pm}$ ), Bruggeman coefficient ( $Br_+$ ), kinetic rate constants ( $k_{\pm}$ ), active material particle radius ( $r_+$ ), electrode porosity ( $\epsilon_-$ ) and SEI-layer thickness ( $w_{sei}$ ). b) Measured voltage profile when running all optimal experiments during a cell charge.

### 3.2.2 Parameterization in the frequency domain

With available EIS data for the NMC/Gr cells showing significant changes with battery degradation, the idea of simulating the impedance spectra with a physics-based model emerged. In Paper IV, a parameterization method combining frequency-domain data (varying the current over different frequencies) and time-domain data (varying the current over time) was developed. The initial attempt was to fit eleven dynamic parameters to the impedance spectra and validate the model with a time-domain simulation. The plan changed as the electrolyte diffusivity  $D_l$  was found to have a low sensitivity in the frequency domain, but a high sensitivity in the time domain. This resulted in a parameterization method including two steps. The first step

included fitting ten dynamic parameters to EIS data: intercalation diffusivity ( $D_{\pm}$ ), Bruggeman coefficient ( $Br_{\pm}$ ), exchange current density ( $i_{0,\pm}$ ), double layer capacitance ( $C_{dl,\pm}$ ), electrolyte conductivity ( $\kappa$ ) and a lumped resistance ( $R_{cc}$ ), (see Figure 17a). In a second step, the time-domain profile (Figure 17b) was used to fit  $D_I$ .

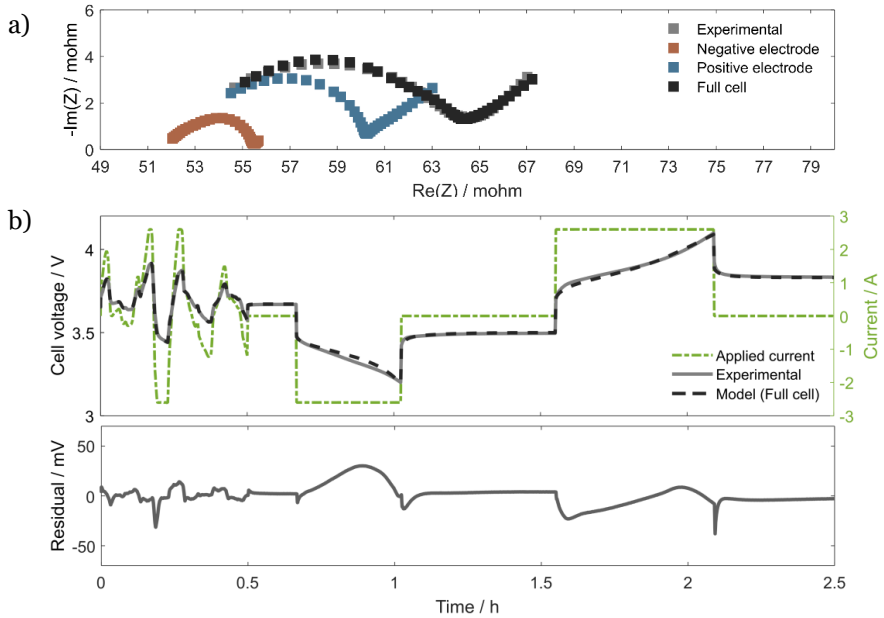


Figure 17: Parameterization results and validation for a beginning of life (BOL) reference cell (NMC/Gr). a) impedance measured at 50% SOC b) Time-domain validation profile. c) The difference between the simulated voltage and the experimental data. Adapted from Paper IV.

### 3.2.2.1 Evaluation of simplified models

With a parameterization strategy resulting in accurate parameters in both the time and frequency domains, our two simplified models were further evaluated in Paper V. The Electrolyte model showed a small loss of accuracy when ignoring the polarization due to the solid phase diffusion during longer periods of charge and discharge, at a 1C-rate. For the same current trajectory, the SPM showed almost double the increase in the model error when ignoring polarization due to the liquid-phase diffusion. These findings support our results from the sensitivity analysis that electrolyte mass transport dominates the voltage behavior compared to the solid-phase mass transport, even at a rate of 1C. In the next step we reparameterized the diffusion coefficients of the simplified models against the time-domain data, which is usually the approach when evaluating new models. A good fit to the experimental data was obtained

for both models, but their differences were made clear when the models were validated in the frequency domain by EIS simulations, seen in Figure 18. While the Electrolyte model underestimates the low frequency impedance and does not fully capture the total polarization, the SPM overestimates the polarization effects from the solid phase diffusion. Both simplified models were therefore discarded, as the correct physical processes were not captured.

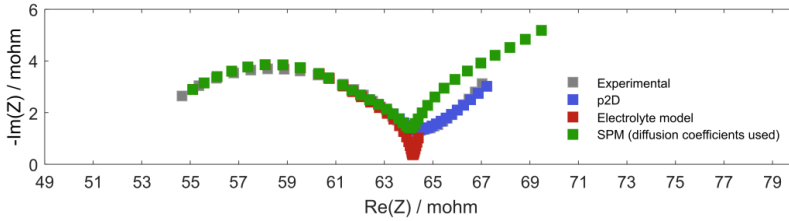


Figure 18: Evaluation of the two simplified physics-based models, compared to the p2D model and experimental data. The p2D model is used for all simulations and only the parameters for the diffusion processes are changed. Parameters for the diffusion processes have been obtained from parameterization in the time domain. Adapted from Paper V.

### 3.2.3 Parameter re-evaluation with battery aging

After having developed an efficient and accurate parameterization strategy based on the optimal experiments, the evolution of these parameters with battery aging was studied in Paper III. Since capacity loss and power fade will have a direct impact on the voltage profile, the goal was to, through re-evaluation of the parameters, better understand the internal degradation mechanisms. As this approach is non-invasive, it can also be used to monitor the cells and avoid cycling in regions where certain mechanisms are accelerated.

The eight experiments designed in Paper II were still used, and the same processes were targeted, but some adjustments were made to the parameter value estimations. The tortuosity for both electrodes  $\tau_{\pm}$  was now fitted directly, rather than via the Bruggeman coefficient ( $Br_{+}$ ) and the negative electrode porosity  $\varepsilon_{-}$  (this coupling is described in Equation 2.11). Furthermore, the diffusion time constant for each electrode  $\Delta t_{\pm}$  is now fitted, which is the lumped contribution from the diffusion length (particle radii) and the diffusion coefficient, see Equation 2.10. The motivation is to achieve the same parameter accuracy but with a faster fitting procedure and fewer couplings between the parameters to solve for. The SEI-layer thickness parameter was discarded, due to its low sensitivity. Lastly a lumped resistance parameter  $R_{cc}$  was added, that is neither distributed in the porous electrode nor has SOL dependency.

In the following chapters the obtained parameters and the degradation trends will be analysed and compared between the different methods. That includes

the electrochemical degradation analysis in Paper I, the optimal experiment fitting in Paper III and the impedance fitting in Paper IV.

### 3.2.3.1 Thermodynamic parameters

The thermodynamic behaviour of the cells has been analysed, both through the electrochemical technique DVA, as well as through the electrode balancing step in the model parameterization. In the electrode balancing, the model is fitted to a C/20 discharge curve and  $SOL_{\max/\min,\pm}$  can be estimated as previously demonstrated in Figure 4. Voltage changes in the discharge curve can be hard to see, and therefore DVA is performed by differentiating the voltage data with respect to the discharged capacity. With a suitable smoothing algorithm, signature slopes and plateaus from each electrode can be identified and the electrode health evaluated. Different results are obtained from the different methods and will therefore be further elaborated on.

The thermodynamic parameters updated in the p2D model are the electrode active material volume fractions  $\varepsilon_{s,\pm}$  and initial electrode lithium concentrations  $c_{\text{init},\pm}$ . Three sources of capacity loss are found in LiBs (LAM<sub>PE</sub>, LAM<sub>NE</sub> and LLI) and their effect on the model parameters will be explained. LAM<sub>PE/NE</sub> forces a wider operating window of the electrode, hence  $SOL_{\max,\pm}$  will increase,  $SOL_{\min,\pm}$  will decrease, or both. These changes result in a decrease of  $\varepsilon_{s,\pm}$ , as seen in Equation 2.3. If the capacity loss is due to LLI, returning to Equation 2.3,  $Q_{\text{cell}}$  will decrease and the operating window of the electrode will shrink as well keeping the ratio  $Q_{\text{cell}}/(SOL_{\max,\pm} - SOL_{\min,\pm})$  unchanged. As a result,  $\varepsilon_{s,\pm}$  does not change but the total available lithium content decreases, following Equation 2.7. In the electrochemical DVA (Paper I), the capacity of the negative electrode was unchanged for all cells. Though signs of LAM<sub>PE</sub> were seen for PS<sub>1C</sub> and FRPS<sub>2C</sub>, the main capacity loss was attributed to LLI. However, from the parameterization in Paper III, a similar trend of LLI, LAM<sub>PE</sub>, and LAM<sub>NE</sub> is seen, following the capacity loss. This is shown in Figure 19a where  $\eta_{s,+}$ ,  $\varepsilon_{s,+}$  and  $\varepsilon_{s,-}$  result from the balancing. The normalized amount of cyclable lithium  $\eta_{s,+}=1$ , means the same rate of LLI as LAM<sub>PE</sub> according to Equation 2.4. The parameterization results in Paper IV also deviate from the electrochemical DVA analysis. The same rate of LLI and LAM<sub>PE</sub> is observed (slightly faster than LAM<sub>NE</sub>), shown in Figure 19b. These results deserve some reflection, as it appears somewhat surprising that the parameterization (with good fits to the experimental data), show different results than the DVA analysis of the same data. It seems that the optimization solver captures the changes with the capacity decrease but fails to distinguish correct values for  $SOL_{\max/\min,\pm}$ . Defining the initial and final potential of the electrodes from a discharge curve comes with several challenges. At 100%

SOC, the half cell potential curves are rather flat, hence many solutions might exist for  $U_+ - U_-$  to match the cell voltage. The second problem is the cell polarization that might have influence even at low currents, especially at low SOC due to the steep OCP. This effect will also get worse as the cells degrade. Analysing thermodynamic degradation modes from physics-based model fitting should therefore be performed with caution. The active material volume fractions also determine the active surface area of the electrodes in the model. Hence, incorrect parameterization will also indirectly affect the values of the kinetic rate constants.

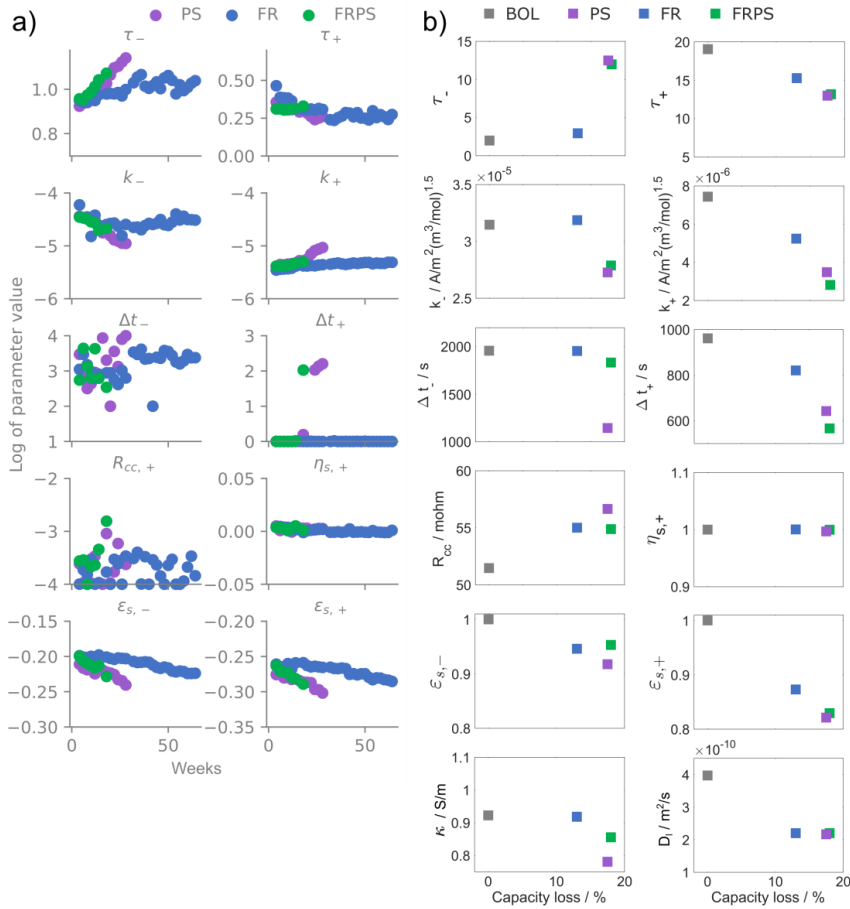


Figure 19: Parameter evolution with NMC/Gr cell degradation, comparison of the parameterization strategy a) Optimal experiments (reproduced from Paper III) and b) EIS (Paper IV). a) Re-parameterization through optimal experiments until 10% capacity loss for PS, 8% for FRPS and 4% for FR. b) Parameterization from impedance data at the final stage of degradation, capacity shown on the x-axis.

### 3.2.3.2 Dynamic parameters

As the dynamic parameters for the same cells during aging have been determined through two different parameterization approaches (Paper III, fitting to the optimal experiments, and Paper IV, fitting to EIS), the comparison between the values will be discussed. The two studies were performed at different stages in the battery lifetime, the data for Paper III was collected one year before the data in Paper IV, but a comparison between the two methods can still be made.

The optimal experiments were applied to PS<sub>1C</sub>, FRPS<sub>2C</sub>, and FR<sub>1C</sub> as part of the RPTs in the degradation study. The maximum capacity loss was seen for PS (10%), followed by FRPS (8%) and FR (4%). The repeated re-parameterization and resulting parameter trajectories can be seen in Figure 19a. The cells were later repurposed for the milder FR<sub>1.5</sub> application and further degraded in Paper IV. The results from the re-parameterization at end of test (EOT) are shown in Figure 19b, when fitting the model to impedance data. The cells have reached different levels of degradation at EOT in this study and are plotted in the order of capacity loss. Figure 19b also includes a fresh BOL reference cell (at 0% capacity loss), this value should be comparable to the start of the cycling in Figure 19a (week 0). Note that the values in Figure 19a are plotted on a logarithmic scale.

Most parameters show a trend with decreasing/increasing parameter value with capacity loss in Figure 19b. The negative electrode tortuosity  $\tau_-$  increases in both studies. FR<sub>1C</sub> only shows a slight increase even after 10% capacity loss while PS<sub>1C</sub> and FRPS<sub>2C</sub> experience a large increase. Interestingly, both studies also show a decrease in  $\tau_+$ . An increase in the positive electrode thickness has been measured before, which could explain the decrease in tortuosity [15], [50], [51], [52].

The kinetic evolution (here expressed as rate constants including the electrolyte concentration  $k_{\pm} = \hat{k}_{\pm}F/\sqrt{c_{e,0}}$ ) shows a decrease for both the positive and negative electrode in Figure 19b. The decrease of  $k_-$  in Figure 19a is much larger though. Figure 19a also shows a slight increase in  $k_+$ , which can be one reason for the difference. Another explanation is that in Paper IV we also updated the electrolyte conductivity ( $\kappa$ ) to capture a decreasing conductivity as the cells degrade (down to -15%). Polarization due to this fast process can be hard to separate from the kinetic contribution in the time-domain. Separating the contributions of the kinetics at the positive and negative electrodes also remains a challenge. In Paper II, we concluded from sensitivity analysis that even when designing single parameter targeted optimal experiments,  $k_+$  and  $k_-$  were equally sensitive to both. Hence concluding electrode-specific degradation of the reaction kinetics should be done with caution. As mentioned before, these values are also coupled to the

specific surface area, partly determined by the electrode balancing. In the case of an overestimation of loss of active material, as discussed in the previous section, kinetic limitations will be underestimated. The result of a decreased kinetic rate constant is therefore reliable. This might stem from changes at the interface of the particle surface due to surface layers or degradation of the active material itself.

When evaluating the particle diffusion time constants, in Figure 19a,  $\Delta t_-$  shows a rather noisy result during the whole experiment and  $\Delta t_+$  only starts to affect the performance in the last measurements for PS<sub>1C</sub> and FRPS<sub>2C</sub>. The optimal experiment for  $\Delta t_-$  was designed at a very low SOC. At these potentials, the time for the cell to reach equilibrium is longer than for the medium SOC regions and the relaxation time needed is often increased as the cells degrade. Longer periods of rest before the measurement could therefore have improved the parameterization. In Figure 19b, the diffusion time constants are obtained from EIS data where the frequency dependency better separates the contribution from the different processes and the measurement is performed at steady state (after a 3 h rest). Here, a decreasing time constant (faster diffusion) is seen for both electrodes but the positive electrode shows the biggest change. The EIS is only measured at 50% SOC, at high and low SOC the trend might be different. Additionally, we re-parameterized the electrolyte diffusion coefficient  $D_l$  in Paper IV, which showed a maximum decrease in diffusivity of 45%. Finally, the lumped resistance term ( $R_{cc}$ ) showed an increasing trend with aging in both studies.

To sum up, we see a large increase in the negative electrode tortuosity from both methods. This results in the largest parameter changes as the effective electrolyte diffusivity in the negative electrode decreases by 90% for FRPS<sub>2C</sub> and the effective conductivity by 85% (Paper IV). This highlights the importance of updating the electrolyte mass transport properties as the batteries degrade.

The kinetic rate constants, as well as the lumped resistance term, all contribute to the fast dynamic response of the battery. An advantage of EIS is that purely resistive behavior (such as  $R_{cc}$ ), can be separated from processes including capacitive behavior (such as redox reactions and double layer charging). Decoupling the kinetic contributions from each electrode ( $k_+$ ,  $k_-$ ) remains a challenge with both methods and possible parameter interplay can therefore not be excluded.

The solid-phase diffusion does not introduce any major additional polarization with aging from any of the methods. While the jump in  $\Delta t_+$  for PS and FRPS in Figure 19a indicates a decrease in solid-phase diffusivity, our results from Paper IV (showing a decrease in  $D_l$ ), would explain this as an actual decrease in the liquid-phase diffusion and not the solid phase. The challenge with low-SOC

voltage drift and noisy parameter values were also avoided with the EIS fitting method.



## 4 Conclusions

As lithium-ion battery degradation is highly path dependent, there exists a tradeoff between battery performance fade and the delivered power and energy. Milder utilization can prolong the battery lifetime but increase the number of cells needed. On the other hand, with fewer cells, the power and energy limits might be challenged and degradation may be accelerated. As several services are needed to support the power grid, as well as other options for electricity support, understanding the battery degradation coupled to specific services can provide valuable information for grid operators. In the following chapter, I will conclude the main findings on how BESS are best operated, how the battery state of health (SOH) can be evaluated, and finally the sources of the performance fade.

In Paper I we found, as expected, a mild degradation from the Frequency Regulation (FR) service. We further demonstrated the potential to combine FR with a Peak Shaving (PS) service, operating in a wider state of charge window ( $\Delta$ SOC). We found that a higher rate of energy could be delivered, without a higher rate of capacity loss, compared to the single PS service. Stress factors for degradation were analysed in Paper IV and a wide  $\Delta$ SOC operation shown to accelerate the capacity loss more than the increased current amplitude and cell voltage. Differences in the polarization trends were also found. All NMC/Gr cells showed a linear increase in the high frequency resistance (HFR) with capacity loss, but only services with a wide  $\Delta$ SOC and high current (FRPS<sub>2C</sub> and PS<sub>1C</sub>) showed a growth of the semicircle in their impedance spectra as well. FR as a 2<sup>nd</sup> application decreased the capacity loss rate for both the NMC/Gr cells (Paper IV) and the NCA/Gr-SiO<sub>x</sub> cells (Paper VI), while a wider SOC operation highlighted the need for improved initial SOH evaluation to predict the battery lifetime. To conclude, keeping the cells close to 50% SOC if possible and providing short charge/discharge pulses as in FR is the most beneficial type of service in terms of battery lifetime. If BESS is used to support the grid in more demanding services, it is notable that operation for PS, at 1C-rate and

22-78% SOC resulted in the same capacity loss rate as at 0.5C-rate and 38-62% SOC. The higher voltage and current levels could therefore be used without accelerating capacity loss. A larger impedance increase was observed though for the higher current services and an accelerated capacity loss rate or power limitations might occur later in life.

While experimental studies in controlled environments are crucial to develop an understanding of battery degradation, their full-scale operation is more complex. Experimental studies on battery aging alone are therefore insufficient, instead characterization methods from *in situ* measurements need to be applied to evaluate the battery SOH. As voltage and current often are the only signals measurable during normal operation, physics-based models are a valuable tool to obtain additional information of battery internal states and sources of the performance loss. Two simplified models were evaluated in Paper V and found insufficient, as the correct physical processes were not captured. In Papers III and IV, we demonstrate two methods of p2D-model parameterization, capturing crucial internal degradation phenomena by updating parameters and improving model accuracy. In Paper III, one optimal experiment was designed for each targeted parameter, maximizing parameter sensitivity and minimizing interactions with other parameters. The resulting parameter values were validated in terms of identifiability and *ex situ* material characterization. In Paper IV, we take this strategy further, reoptimizing the parameters to not only show accuracy in the time domain, but also in the frequency domain, simulating electrochemical impedance spectroscopy (EIS). We additionally include the electrolyte conductivity and diffusivity to the re-parameterization procedure, as these might also change with battery aging. The obtained results highlight an important aspect often ignored in battery degradation analysis, which is the changing mass transport properties of the electrolyte as solvents are consumed due to side-reactions. Remaining challenges with both parameterization strategies include the separation of the positive and negative electrode charge transfer resistances, as well as a correct estimation of the available capacity in the electrodes (i.e., the electrode balancing). Capacity difference analysis (CDA) is finally suggested as an addition to the SOH metric, capturing degradation related to mass transport limitations. The lower capacity at a higher current is shown to originate from unutilized active material for the degraded NCA/Gr-SiO<sub>x</sub> cells. The high capacity loss rate for cells with a high CDA suggests uneven current distribution further accelerating the degradation.

With several methods applied to analyze battery degradation the mechanisms causing the performance fade, and the stress factors, will finally be discussed. A wide  $\Delta$ SOC operation was found to be the main stress factor for capacity loss for the NMC/Gr cells, in Paper IV. Stress, both in the active material particles and covering surface layers, will be introduced as lithium is (de)intercalated and volume changes occur. Loss of active material ( $LAM_{NE/PE}$ ) due to this stress, would affect the active surface area and also be seen in EIS data as an

increase of the semicircle width in the Nyquist plot. This is not observed for all the cells losing capacity at the higher rate and loss of cyclable lithium inventory (LLI) is therefore believed to be the main driver for the capacity loss. SEI-layer growth, consuming  $\text{Li}^+$ , is triggered by a low potential of the negative electrode. SEI-layer growth can be further be accelerated as volume changes cause cracks in the layer and/or particles and fresh surface gets exposed to the electrolyte [26].

An increase in the negative electrode tortuosity with aging as well as a decrease in the positive electrode tortuosity was seen from both parameterization methods. We link these trends to SEI-layer growth on the negative electrode and cracks of the particles in the positive electrode, resulting in an electrode thickness increase (confirmed by scanning electron microscopy in Paper III). SEI-layer growth also consumes electrolyte solvents and effects due to that have been identified with parameter fitting to impedance data and CDA. In Paper IV, we found electrolyte conductivity decreased by -15% for the most heavily degraded cell and electrolyte diffusivity decreased by -45%. In Paper VI, a high CDA value was demonstrated to result from mass transport limitations and unutilized active material. This can either stem from a low electrolyte diffusivity, or slow lateral transport of lithium due to, for example electrolyte depletion or separator damage.

## Outlook

After the conducted analysis on battery degradation and comparison of methods for characterization, some reflections on the direction of future research will be shared.

First, BESS utilization will depend on many factors. Economic incentives, prediction of future electricity needs, as well as other possible support solutions. Our results highlight beneficial ways to utilize the batteries from a degradation perspective. While this controlled cycling will not be the case in full-scale operation, the results can serve as a guideline or input in models including additional factors in grid operation.

Second, while two parameterization methods have been demonstrated in this thesis, to obtain degradation related information, further improvements to both methods can still be made. Parameter interactions, as well as biased values, are very complex problems. While extensive work was performed when designing and evaluating the optimal experiments, assumptions still had to be made (for example, the constant electrolyte mass transport properties). This will further affect the values obtained through parameterization, as the wrong parameters might instead capture these effects. The parameter accuracy was improved as the parameters were re-evaluated to also fit the impedance spectra. After demonstrating the possibility to parameterize against impedance spectra, a more general approach, suitable also for other cell types, should be

developed. Additional validation, proving parameter identifiability in the frequency domain, is also needed.

Third, battery degradation analysis is often conducted with the electrodes in focus. Electrode sheets can be harvested after cycling for investigation with microscopical techniques and further electrochemical cycling by reassembly with a reference electrode and fresh electrolyte. While this analysis can provide insights when compared with an unaged cell, the electrolyte degradation effects are completely lost and misleading conclusions about the sources of the battery performance loss might be drawn. Our results show that focus also needs to be put on the change in mass transport properties of the electrolyte and methods to evaluate this as the cells degrade.

Finally, we see an effect of unutilized electrode material as the cells degrade. To understand this effect further, battery degradation models are needed that solve for more than one dimension of the electrode. Effects of separator dry out and the lateral flow of lithium can then better be understood and hopefully avoided.

# Acknowledgements

This work would never have happened if it wasn't for my supervisors. Thank you for believing in me, supporting me and giving me this opportunity to grow as a person and scientist. Göran thank you for sharing your endless curiosity for science, your great knowledge in electrochemistry and slowly making me love both impedance data and physics-based modelling. Raket thank you for pushing me to find new research questions, analyzing the data from all perspectives and improving my skills in communicating research. You have always had the door open and offered support in all forms. Although not my supervisor on paper, thank you Henrik for taking on all my questions and struggles when starting to work with battery models. You have made the world of multiphysics a little bit less complicated and overwhelming. Sophie, Magnus, Firas and Jinying thank you for your time, input and fruitful discussions!

I would not have made it all the way through if I did not get to share the ups and downs of a PhD journey with all my amazing colleagues. Moritz, I am forever grateful for my start sharing office, struggles and fun moments with you. Thank you for letting me follow in your footsteps, all the discussions on degradation and parameterization and your support as a friend. Our lab hero and my dear friend Alex, your helpfulness, positive attitude and battery knowledge have truly been a guiding light for me. Thank you Jai for spreading love, laughs and all the good gossip. My time at TEK would not have been the same without you!

Thank you Deniz for your friendship, honesty and support during these years. My office mates, Henrik and Darius, it has been a great pleasure! Thank you Martina for fun times at and outside the office! Finally thank you Eva for many good times, but especially sharing this last sprint of the PhD journey together. The excitement, stress and confusion have been so much easier to handle with you by my side! And to all the other crazy researchers I have had the pleasure to meet during these years, thank you and I wish you all the best in the future!

To my crew outside the brick walls of KTH. Margit, Astrid, Åsa, Sigge, Isak, Roxy and Karin, what better way to balance hard work than to dance the night away with you! And to Ebba, Linnea, Amanda, Anna, Johanna and Margit who was there in Lund when the engineering journey started. I am forever grateful for all our good times and your support during these roller-coaster years!

Finally, to my mum and dad. With your endless support and love I have dared to challenge myself, trust my instincts and become a version of myself that I am truly proud of. Nothing makes me happier than getting to celebrate this achievement together with you!

## References

- [1] "CO<sub>2</sub> Emissions in 2022", IEA, Paris, 2023. <https://www.iea.org/reports/co2-emissions-in-2022>
- [2] "Batteries and Secure Energy Transitions", IEA, Paris, 2024. <https://www.iea.org/reports/batteries-and-secure-energy-transitions>
- [3] "From Taking Stock to Taking Action", IEA, Paris, 2024. <https://www.iea.org/reports/from-taking-stock-to-taking-action>
- [4] IRENA, 'Electricity Storage and Renewables: Costs and Markets to 2030', International Renewable Energy Agency, Abu Dhabi, 2017.
- [5] U.S. Energy Information Administration, 'International Energy Outlook 2023', Oct. 2023.
- [6] IEA, 'Global installed grid-scale battery storage capacity in the Net Zero Scenario, 2015-2030, IEA, Paris', IEA. Licence: CC BY 4.0. [Online]. Available: <https://www.iea.org/data-and-statistics/charts/global-installed-grid-scale-battery-storage-capacity-in-the-net-zero-scenario-2015-2030>
- [7] D. Kucevic *et al.*, 'Standard battery energy storage system profiles: Analysis of various applications for stationary energy storage systems using a holistic simulation framework', *J. Energy Storage*, vol. 28, p. 101077, Apr. 2020, doi: 10.1016/j.est.2019.101077.
- [8] J. Vetter *et al.*, 'Ageing mechanisms in lithium-ion batteries', *J. Power Sources*, vol. 147, no. 1, pp. 269–281, Sep. 2005, doi: 10.1016/j.jpowsour.2005.01.006.
- [9] J. S. Edge *et al.*, 'Lithium ion battery degradation: what you need to know', *Phys. Chem. Chem. Phys.*, vol. 23, no. 14, pp. 8200–8221, Apr. 2021, doi: 10.1039/D1CP00359C.
- [10] J. Urquizo and P. Singh, 'A review of health estimation methods for Lithium-ion batteries in Electric Vehicles and their relevance for Battery Energy Storage Systems', *J. Energy Storage*, vol. 73, p. 109194, Dec. 2023, doi: 10.1016/j.est.2023.109194.
- [11] S. Gustafsson, 'The Nobel Prize in Chemistry 2019', The Royal Swedish Academy of Sciences, 2019.
- [12] J.-J. Marie and S. Gifford, 'Developments in lithium-ion battery cathodes', *Faraday Insights*, no. 18, 2023.
- [13] S. He, S. Huang, S. Wang, I. Mizota, X. Liu, and X. Hou, 'Considering Critical Factors of Silicon/Graphite Anode Materials for Practical High-Energy Lithium-Ion Battery Applications', *Energy Fuels*, vol. 35, no. 2, pp. 944–964, Jan. 2021, doi: 10.1021/acs.energyfuels.0c02948.
- [14] M. Armand *et al.*, 'Lithium-ion batteries – Current state of the art and anticipated developments', *J. Power Sources*, vol. 479, p. 228708, Dec. 2020, doi: 10.1016/j.jpowsour.2020.228708.

- [15] A. Mikheenkova *et al.*, ‘Ageing of High Energy Density Automotive Li-Ion Batteries: The Effect of Temperature and State-of-Charge’, *J. Electrochem. Soc.*, vol. 170, no. 8, p. 080503, Aug. 2023, doi: 10.1149/1945-7111/aceb8f.
- [16] A. J. Smith *et al.*, ‘Localized lithium plating under mild cycling conditions in high-energy lithium-ion batteries’, *J. Power Sources*, vol. 573, p. 233118, Jul. 2023, doi: 10.1016/j.jpowsour.2023.233118.
- [17] J. Sieg *et al.*, ‘Local degradation and differential voltage analysis of aged lithium-ion pouch cells’, *J. Energy Storage*, vol. 30, p. 101582, Aug. 2020, doi: 10.1016/j.est.2020.101582.
- [18] M. J. Mühlbauer *et al.*, ‘Inhomogeneous distribution of lithium and electrolyte in aged Li-ion cylindrical cells’, *J. Power Sources*, vol. 475, p. 228690, Nov. 2020, doi: 10.1016/j.jpowsour.2020.228690.
- [19] X. Zhou, J. Huang, Z. Pan, and M. Ouyang, ‘Impedance characterization of lithium-ion batteries aging under high-temperature cycling: Importance of electrolyte-phase diffusion’, *J. Power Sources*, vol. 426, pp. 216–222, Jun. 2019, doi: 10.1016/j.jpowsour.2019.04.040.
- [20] S. M. Kuzovchikov *et al.*, ‘Electrolyte refilling as a way to recover capacity of aged lithium-ion batteries’, *J. Power Sources*, vol. 601, p. 234257, May 2024, doi: 10.1016/j.jpowsour.2024.234257.
- [21] I. Bloom *et al.*, ‘Differential voltage analyses of high-power, lithium-ion cells’, *J. Power Sources*, vol. 139, no. 1–2, pp. 295–303, Jan. 2005, doi: 10.1016/j.jpowsour.2004.07.021.
- [22] I. Bloom, L. K. Walker, J. K. Basco, D. P. Abraham, J. P. Christophersen, and C. D. Ho, ‘Differential voltage analyses of high-power lithium-ion cells. 4. Cells containing NMC’, *J. Power Sources*, vol. 195, no. 3, pp. 877–882, Feb. 2010, doi: 10.1016/j.jpowsour.2009.08.019.
- [23] S. J. Cooper, A. Bertei, D. P. Finegan, and N. P. Brandon, ‘Simulated impedance of diffusion in porous media’, *Electrochimica Acta*, vol. 251, pp. 681–689, Oct. 2017, doi: 10.1016/j.electacta.2017.07.152.
- [24] W. Hu, Y. Peng, Y. Wei, and Y. Yang, ‘Application of Electrochemical Impedance Spectroscopy to Degradation and Aging Research of Lithium-Ion Batteries’, *J. Phys. Chem. C*, vol. 127, no. 9, pp. 4465–4495, Mar. 2023, doi: 10.1021/acs.jpcc.3c00033.
- [25] T. F. Fuller, M. Doyle, and J. Newman, ‘Simulation and Optimization of the Dual Lithium Ion Insertion Cell’, *J. Electrochem. Soc.*, vol. 141, no. 1, p. 1, Jan. 1994, doi: 10.1149/1.2054684.
- [26] J. M. Reniers, G. Mulder, and D. A. Howey, ‘Review and Performance Comparison of Mechanical-Chemical Degradation Models for Lithium-Ion Batteries’, *J. Electrochem. Soc.*, vol. 166, no. 14, p. A3189, Sep. 2019, doi: 10.1149/2.0281914jes.

- [27] P. M. Attia *et al.*, ‘Review—“Knees” in Lithium-Ion Battery Aging Trajectories’, *J. Electrochem. Soc.*, vol. 169, no. 6, p. 060517, Jun. 2022, doi: 10.1149/1945-7111/ac6d13.
- [28] M. Dubarry, A. Devie, K. Stein, M. Tun, M. Matsuura, and R. Rocheleau, ‘Battery Energy Storage System battery durability and reliability under electric utility grid operations: Analysis of 3 years of real usage’, *J. Power Sources*, vol. 338, pp. 65–73, Jan. 2017, doi: 10.1016/j.jpowsour.2016.11.034.
- [29] M. Dubarry and A. Devie, ‘Battery durability and reliability under electric utility grid operations: Representative usage aging and calendar aging’, *J. Energy Storage*, vol. 18, pp. 185–195, Aug. 2018, doi: 10.1016/j.est.2018.04.004.
- [30] A. J. Crawford *et al.*, ‘Lifecycle comparison of selected Li-ion battery chemistries under grid and electric vehicle duty cycle combinations’, *J. Power Sources*, vol. 380, pp. 185–193, Mar. 2018, doi: 10.1016/j.jpowsour.2018.01.080.
- [31] M. Elliott, L. G. Swan, M. Dubarry, and G. Baure, ‘Degradation of electric vehicle lithium-ion batteries in electricity grid services’, *J. Energy Storage*, vol. 32, p. 101873, Dec. 2020, doi: 10.1016/j.est.2020.101873.
- [32] N. Kim *et al.*, ‘Comparison of Li-ion battery chemistries under grid duty cycles’, *J. Power Sources*, vol. 546, p. 231949, Oct. 2022, doi: 10.1016/j.jpowsour.2022.231949.
- [33] G. Baure and M. Dubarry, ‘Battery durability and reliability under electric utility grid operations: 20-year forecast under different grid applications’, *J. Energy Storage*, vol. 29, p. 101391, Jun. 2020, doi: 10.1016/j.est.2020.101391.
- [34] S. J. Tong, A. Same, M. A. Kootstra, and J. W. Park, ‘Off-grid photovoltaic vehicle charge using second life lithium batteries: An experimental and numerical investigation’, *Appl. Energy*, vol. 104, pp. 740–750, Apr. 2013, doi: 10.1016/j.apenergy.2012.11.046.
- [35] J. Lacap, J. W. Park, and L. Beslow, ‘Development and Demonstration of Microgrid System Utilizing Second-Life Electric Vehicle Batteries’, *J. Energy Storage*, vol. 41, p. 102837, Sep. 2021, doi: 10.1016/j.est.2021.102837.
- [36] B. Gohla-Neudecker, M. Bowler, and S. Mohr, ‘Battery 2nd life: Leveraging the sustainability potential of EVs and renewable energy grid integration’, in *2015 International Conference on Clean Electrical Power (ICCEP)*, Jun. 2015, pp. 311–318. doi: 10.1109/ICCEP.2015.7177641.
- [37] W. Gao, Z. Cao, N. V. Kurdkandi, Y. Fu, and C. Mi, ‘Evaluation of the second-life potential of the first-generation Nissan Leaf battery packs in energy storage systems’, *eTransportation*, vol. 20, p. 100313, May 2024, doi: 10.1016/j.etrans.2024.100313.
- [38] D. R. Conover *et al.*, ‘Protocol for Uniformly Measuring and Expressing the Performance of Energy Storage Systems’.
- [39] K. Frenander and T. Thiringer, ‘Low Frequency influence on degradation of commercial Li-ion battery’, *Electrochimica Acta*, vol. 462, p. 142760, Sep. 2023, doi: 10.1016/j.electacta.2023.142760.

- [40] Y. Li *et al.*, ‘A quick on-line state of health estimation method for Li-ion battery with incremental capacity curves processed by Gaussian filter’, *J. Power Sources*, vol. 373, pp. 40–53, Jan. 2018, doi: 10.1016/j.jpowsour.2017.10.092.
- [41] A. J. Smith, P. Svens, M. Varini, G. Lindbergh, and R. W. Lindström, ‘Expanded In Situ Aging Indicators for Lithium-Ion Batteries with a Blended NMC-LMO Electrode Cycled at Sub-Ambient Temperature’, *J. Electrochem. Soc.*, vol. 168, no. 11, p. 110530, Nov. 2021, doi: 10.1149/1945-7111/ac2d17.
- [42] J. Landesfeind and H. A. Gasteiger, ‘Temperature and Concentration Dependence of the Ionic Transport Properties of Lithium-Ion Battery Electrolytes’, *J. Electrochem. Soc.*, vol. 166, no. 14, p. A3079, Sep. 2019, doi: 10.1149/2.0571912jes.
- [43] L. O. Valøen and J. N. Reimers, ‘Transport Properties of LiPF<sub>6</sub>-Based Li-Ion Battery Electrolytes’, *J. Electrochem. Soc.*, vol. 152, no. 5, p. A882, Mar. 2005, doi: 10.1149/1.1872737.
- [44] M. Streb, M. Andersson, V. Löfqvist Klass, M. Klett, M. Johansson, and G. Lindbergh, ‘Investigating re-parametrization of electrochemical model-based battery management using real-world driving data’, *eTransportation*, vol. 16, p. 100231, Apr. 2023, doi: 10.1016/j.etrans.2023.100231.
- [45] S. Santhanagopalan, Q. Guo, P. Ramadass, and R. E. White, ‘Review of models for predicting the cycling performance of lithium ion batteries’, *J. Power Sources*, vol. 156, no. 2, pp. 620–628, Jun. 2006, doi: 10.1016/j.jpowsour.2005.05.070.
- [46] P. Keil *et al.*, ‘Calendar Aging of Lithium-Ion Batteries: I. Impact of the Graphite Anode on Capacity Fade’, *J. Electrochem. Soc.*, vol. 163, no. 9, pp. A1872–A1880, 2016, doi: 10.1149/2.0411609jes.
- [47] J. Sieg *et al.*, ‘Fast-charging capability of lithium-ion cells: Influence of electrode aging and electrolyte consumption’, *Appl. Energy*, vol. 305, 2022, doi: 10.1016/j.apenergy.2021.117747.
- [48] N. R. Chowdhury, A. J. Smith, K. Frenander, A. Mikheenkova, R. W. Lindström, and T. Thiringer, ‘Influence of state of charge window on the degradation of Tesla lithium-ion battery cells’, *J. Energy Storage*, vol. 76, p. 110001, Jan. 2024, doi: 10.1016/j.est.2023.110001.
- [49] M. Lewerenz, A. Warnecke, and D. U. Sauer, ‘Introduction of capacity difference analysis (CDA) for analyzing lateral lithium-ion flow to determine the state of covering layer evolution’, *J. Power Sources*, vol. 354, pp. 157–166, Jun. 2017, doi: 10.1016/j.jpowsour.2017.04.043.
- [50] M. Streb, M. Ohrelus, A. Siddiqui, M. Klett, and G. Lindbergh, ‘Diagnosis and prognosis of battery degradation through re-evaluation and Gaussian process regression of electrochemical model parameters’, *J. Power Sources*, vol. 588, p. 233686, Dec. 2023, doi: 10.1016/j.jpowsour.2023.233686.
- [51] K. Jalkanen, J. Karppinen, L. Skogström, T. Laurila, M. Nisula, and K. Vuorilehto, ‘Cycle aging of commercial NMC/graphite pouch cells at different

temperatures', *Appl. Energy*, vol. 154, pp. 160–172, Sep. 2015, doi:  
10.1016/j.apenergy.2015.04.110.

- [52] J. Zhu *et al.*, 'Investigation of lithium-ion battery degradation mechanisms by combining differential voltage analysis and alternating current impedance', *J. Power Sources*, vol. 448, p. 227575, Feb. 2020, doi:  
10.1016/j.jpowsour.2019.227575.